Materials & Design 249 (2025) 113548

Contents lists available at ScienceDirect

Materials & Design

journal homepage: www.elsevier.com/locate/matdes

Effect of boundary conditions on residual stress in cold metal transfer-based wire arc additively manufactured steel components

Xiongfeng Ruan [a,b,*], Burak Karabulut [a], Scott MacDonald [c], Jelena Dobrić [d], Barbara Rossi [a,b]

[a] KU Leuven, Faculty of Engineering Technology, Sint-Katelijne-Waver, Belgium
[b] University of Oxford, Department of Engineering Science, Oxford, United Kingdom
[c] Whittaker Engineering, Robotic Welding Engineering, Stonehaven, United Kingdom
[d] University of Belgrade, Faculty of Civil Engineering, Belgrade, Serbia

ARTICLE INFO

Keywords:
Wire arc additive manufacturing
3Dprint AM35
Numerical modelling
Residual stress pattern

ABSTRACT

This research focusses on wire arc additive manufacturing (WAAM) of carbon steel components made of 3Dprint AM35 (grade S355) by cold metal transfer-based welding process. A finite element (FE) model is developed to simulate the deposition process, and the numerical results are rigorously validated against experimental measurements, demonstrating that the temperature, deformation, and stress fields developing during the additive process can be reproduced accurately. The sensitivity of the FE model to ambient temperature, element activation strategies, alignment errors of thermocouples and strain gauges, and the use of a sequentially coupled approach is analysed. The effect of boundary conditions on the longitudinal and transverse residual stress patterns is studied, revealing that they are highly sensitive to the bolt pretension forces and substrate joining methods. However, they redistribute in a similar manner after the removal of the substrate. Guidance is provided to monitor the residual stress distribution in the fabricated component.

1. Introduction

1.1. Wire arc additive manufacturing

With structural optimisation, the need for less resource-intensive structures, and more complex geometries are designed, which challenges traditional manufacturing methods, and regrettably, forging or casting [1–4], both costly and with limited design flexibility, must be favoured. Through additive deposition of metal inert gas welding, one can create intricate shapes, even with re-entrant angles [5], and achieve unprecedented levels of efficiency [6,7]. Each welding pass adds a single bead of material, and multiple passes erect the three-dimensional component. The additive process of combining an electric arc as heat source and wire as feedstock is usually named wire arc additive manufacturing (WAAM) [8].

Scientific research on WAAM grew exponentially since 2013 [9]. Compared to other additive manufacturing technologies, WAAM has the advantages of lower capital investment (off-the-shelf equipment), higher energy efficiency (around 90 %), and higher deposition rates (0.5 ~ 10 kg/h), leading to even greater efficiency [10–12]. However, during the WAAM deposition process, excessive heat input is introduced into the component, which is prone to severe distortion, residual stress, and dimensional inaccuracy of final products [13]. As a modified WAAM, cold metal transfer (CMT) has better performance as it provides an accurate control of heat input and material deposition by integrating a high-speed digital control and an innovative wire feeding system [14]. The CMT process offers high arc stability, low thermal input, spatter free droplet transfer and high deposition rate [15]. These characteristics make CMT widely used in industries such as automobiles, ships, aerospace, nuclear industry, etc [16].

1.2. State of numerical research on WAAM

Numerical studies on WAAM emerged in 2016, and have received growing attention driven by its potential as a robust, cost-effective, and reliable method for predicting the quality of interests of fabricated components [17]. Research in this area spans various computational scales, from part-scale models that simulate the thermal and deformation cycles [18], to mesoscale models that examine the dynamics of melting pool during deposition [19], and multi-scale models that explore the microstructural evolutions [20]. For instance, Hejripour et al. [21] developed a three-dimensional transient thermal model to

* Corresponding author.
E-mail address: xiongfengruan@gmail.com (X. Ruan).

https://doi.org/10.1016/j.matdes.2024.113548
Received 15 July 2024; Received in revised form 3 November 2024; Accepted 14 December 2024
Available online 15 December 2024

simulate the thermal cycles and cooling rates of WAAM-based duplex stainless steel, which established the relationship between elevated temperatures and microstructure. Cadiou et al. [14] employed a three-dimensional fully coupled approach to model the dynamic behaviour of the filler wire, including its interaction with the molten pool, drop detachment, and deposit growth. Wang et al. [22] created a macro model to simulate the temperature distribution in the weld pool of aluminium alloy, and fed these results into a phase field model to predict the columnar grains growth under different process parameters. These numerical approaches provide valuable insight into thermal development, stress evolution, microstructure formation, defect generation, and other critical phenomena during WAAM processes [17,23,24].

One significant challenge with WAAM is the introduction of severe and non-uniform heat to specimen during deposition, which can result in residual stresses [25]. Residual stresses cause geometric distortions that complexify tolerance management, reduce load-bearing capacity, and promote fatigue failure and stress corrosion cracking [26]. Accurate numerical simulations enable to predict the development of temperature and stress during WAAM, thus monitoring their magnitudes and aiding in quality control of fabricated components. For example, Xiong et al. [27] used a three-dimensional transient heat transfer model, incorporating the element birth and death technique, to investigate the effect of substrate preheating on thermal behaviour. Montevecchi et al. [11] proposed a novel heat source model that considers power distribution between the filler material and base materials, enabling more precise deformation predictions. Additionally, Li et al. [28] studied the impact of different path strategies on residual stress and distortion in laser-CMT hybrid additive manufacturing, and the temperature gradient, residual stress, and distortion of the deposited samples were analysed using the validated model. Despite the advances in modelling accuracy, simulations solving arc physics, mass and heat transfer, solidification, and stress evolution are computationally intensive with current software and hardware capabilities [29]. To alleviate this burden, some researchers have explored alternative numerical strategies, such as the modified inherent strain method [30,31], iterative substructure method [29], dynamic mesh refining method [29,32,33], etc. However, these approaches often involve complex implementations and may not be suitable for intricate engineering structures or complex deposition trajectories. As a result, coupled and uncoupled models remain the standard benchmarks due to their high fidelity and reliability [30,34]. The development of high-fidelity numerical models achieving both accurate and efficiency in WAAM simulation remains challenging, which involves multiple scales and coupled various physical phenomena.

1.3. Research aims and outline of the paper

Low-alloyed carbon steel is well-suited for WAAM applications due to its good weldability, good machineability and excellent strength, which leads to economic and optimized structural designs [35–37]. In this study, we conducted both numerical simulations and experimental investigations to study the effect of boundary conditions on residual stress in multi-layer flat components produced using a CMT-based WAAM process. The wire feed material was 3Dprint AM35 unalloyed carbon steel grade, equivalent to S355. A comprehensive finite element (FE) model was developed and validated against experimentally measured thermal and stress fields evolution. Through a combination of simulation and experimental approaches, we achieved the following objectives: (i) Characterised the temperature fields evolution during the CMT process; (ii) Analysed the stress distributions and residual stress patterns following cooling, unclamping and substrate removal; (iii) Assessed the influence of different boundary conditions on residual stress patterns; (iv) Identified effective strategies to mitigate the residual stresses; and (v) Offered guidelines for predicting residual stress patterns, thereby reducing the need for costly trial and error operations.

The outline of the paper is as follows: Section 2 describes the CMT experimental programme, including detailing specimen preparation, measurements of temperature and strain fields during the process, and profile distortion. Section 3 elaborates on the FE modelling of the CMT process covering model parameters, boundary conditions, governing equations, acquisition of thermal mechanical properties, material deposition modelling, convergence analysis, and characterisation of the heat source model. Section 4 validates the FE results against all experimental measurements for temperature and thermal stress evolution. Section 5 reveals the residual stress redistribution pattern and assesses the sensitivity of the residual stress to boundary conditions such as bolt pretension force and substrate joint methods. Finally, Section 6 draws conclusions and summarizes all important insights into tailoring residual stress.

2. Experiments

2.1. Preparation of the specimens

The industrial welding setup, illustrated in Fig. 1, employed CMT process to fabricate the specimens by means of a Fronius TPS600i power source installed on a 6-axis KR16 R2010 KUKA robot. The voltage and current waveforms are depicted in Fig. 2, at a data acquisition rate of 5 kHz. The average welding power was calculated by integrating and averaging the instantaneous power over time. A 3Dprint AM35 solid wire (Voestalpine Böhler Welding) with diameter of 1.2 mm was selected as welding feed, and the specimens were deposited on a substrate. The substrate was made from S355 steel and was produced through a hot rolling process. To eliminate any residual stress, the substrate underwent a heat treatment at 910 °C with a soaking time of 30 min per inch of thickness. Following heat treatment, the substrate's dimensions and its surface condition were inspected, and no misalignment or surface defects were observed. Additionally, ultrasonic inspection was performed, confirming that the substrate was free of internal defects. The chemical compositions of the feed wire and substrate are listed in Table 1, and their mechanical properties are given in Table 2. The dimensions of the designed components are outlined in Fig. 3. The flat specimens consist of 35 layers, 2 mm each. The substrate was bolted to the platform during the process, and the thickness of the platform was 175 mm. Bolts were tied using a torque wrench and achieving a pretension torque of 29.5 kNm, corresponding to a pretension force of 10.2 kN. Table 3 lists the CMT deposition parameters. To improve deposition quality and avoid lack of fusion, the welding head traced a wave pattern, altering welding start and end points every layer to mitigate overheating and enhance dimensional accuracy. The schematic of the deposition trajectory and welding pass directions is shown in Fig. 4, with a welding sequence repeating itself every 4 layers, with a 3.5 mm stepover and an idle time between adjacent layers of 5 s.

2.2. Temperature measurements

Two complementary techniques were used to measure the temperature development on the welded specimens during metal deposition and cooling stages. Firstly, as shown in Fig. 1, a FLIR thermography camera type A700 captured the thermal field evolution throughout welding and cooling. The view angle of the camera was set to 45° to the front plane of the welded build-up. In addition, 10 K-type thermocouples (TCs) measured the temperature cycles at selected locations. Fig. 5 shows the thermocouples arrangement (blue square) with their corresponding installations in Fig. 6. Thermocouples TC1 to TC4 were embedded beneath the centreline of the weld bead in the substrate at 2 different depths (4 mm and 8 mm). TC5 to TC10 were mounted on the surface of the substrate.

2.3. Measurement of strains and geometrical distortions

Two different techniques were used to measure strain variation and overall distortion of the specimens. Two linear strain gauges (SGs) were

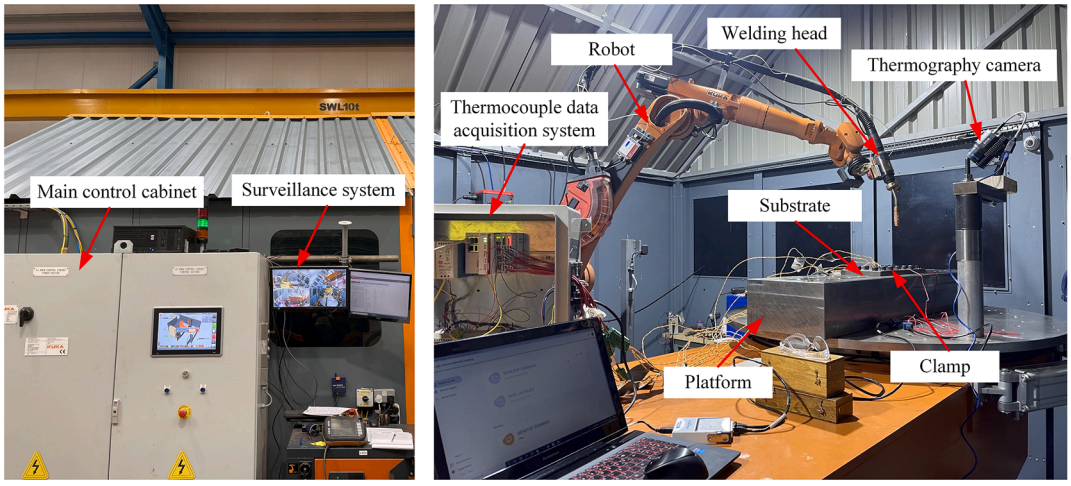

Fig. 1. WAAM equipment and experimental setup.

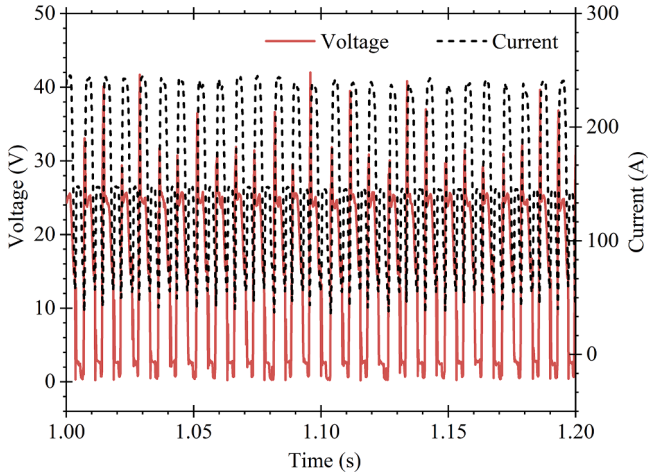

Fig. 2. Measured voltage and current waveforms of CMT process.

glued on the upper surface of the substrate to capture the strain evolution. SG1 was used to measure the longitudinal strain close to the transverse centreline, while SG2 recorded the transverse strain of the longitudinal centreline. The positions of SGs are displayed in Fig. 5. The measured SGs strains were converted to stresses using Hooke's law. In addition, the overall distortion after unclamping was scanned using a three-dimensional laser scanner (3D Design FARO Scan Arm) as depicted in Fig. 7. The 3D scanning accuracy was 0.075 mm for an object size of 2.5 m. To further quantify the scanning accuracy of the laser scanner, four groups of calibration points (CPs) were selected on the top of the substrate. The coordinates of these calibration points (CP1 to CP4) are indicated by red circles in Fig. 5, with each group of calibration points spaced 150 mm apart. The scanning errors for the distances between CPs were −0.448 %, −0.154 %, 0.310 % and −0.077 %, confirming a high level of the scanning accuracy.

3. Finite element modelling

A three-dimensional thermal–mechanical FE model was developed to simulate the thermal cycles, stress development, and deformation across the specimen's 35 layers. For material deposition, the element birth and death technique was applied. Initially deactivated, the finite elements of the specimen are reactivated following the motion pattern of the welding head. In addition, full Newton solution technique was adopted to solve the nonlinear equations. The FE model was built using ABAQUS 2020 solver on a server with two Intel® X®(R) CPU E5-2630 v3 2.40 GHz processors, two NVIDIA Quadro P2000 graphic cards and a 160 GB memory. The graphics processing unit (GPU) acceleration enhanced the convergence by means of allocated GPU cores.

3.1. Governing equations

The first law of thermodynamics is the primary theory underlying the proposed FE model [38]. Heat and mass transfer phenomena in the melting pool were neglected. Therefore, the energy equation valid in the computational domain can be expressed as Equation (1):

$$\frac{\partial(\rho C_P T)}{\partial t} = \frac{\partial}{\partial x}\left(k\frac{\partial T}{\partial x}\right) + \frac{\partial}{\partial y}\left(k\frac{\partial T}{\partial y}\right) + \frac{\partial}{\partial z}\left(k\frac{\partial T}{\partial z}\right) + Q \quad (1)$$

where (x, y, z) are the coordinates of each node in the reference system, T is the corresponding temperature, t is the system time, ρ is the temperature-dependent density, C_P is the specific heat capacity, k is the thermal conductivity, and Q is a source term.

The mechanical problem is governed by the balance of momentum equation, see Equation (2):

Table 2
Mechanical properties of 3Dprint AM35 solid wire and S355 substrate.

Materials	Yield strength $R_{p0.2}$ [MPa]	Tensile strength R_m [MPa]	Elongation A5 [%]
Wire (AM35)	> 355	470 ~ 630	> 22
Substrate (S355)	399	534	33

Table 1
Chemical compositions (wt.%) of 3Dprint AM35 solid wire and S355 substrate.

Materials	C	Si	Mn	P	S	Cr	Mo	Ni	Cu	Fe
Wire (AM35)	0.09	0.30	1.08	0.006	0.005	0.04	0.01	0.03	0.06	Bal.
Substrate (S355)	0.17	0.35	1.20	0.014	0.001	0.04	0.004	0.25	0.22	Bal.

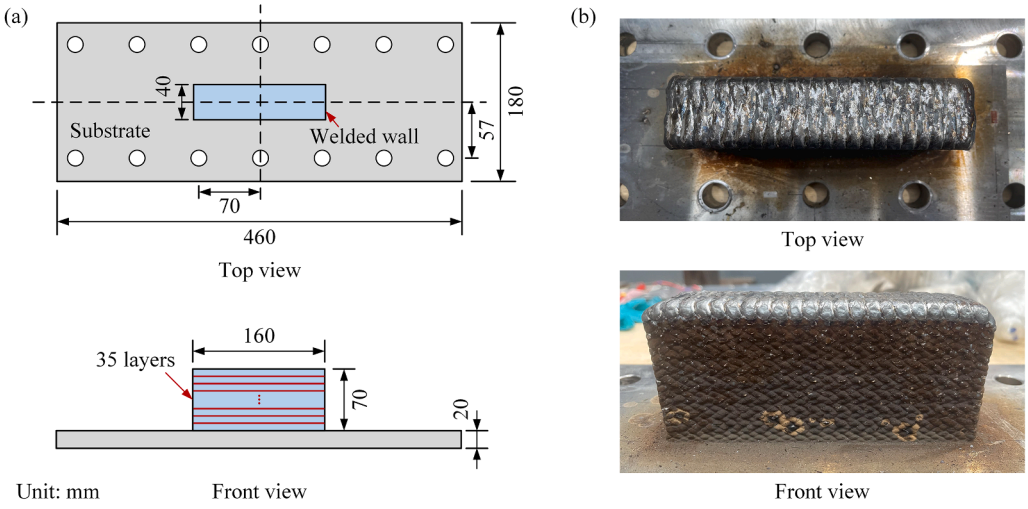

Fig. 3. Schematics of: (a) Designed component; and (b) Manufactured component.

Table 3
CMT deposition parameters.

Parameter	Value
Average power [W]	2500
Deposition speed [m/min]	0.6
Wire feed speed [m/min]	3.6
Contact tip to work distance [mm]	12
Composition of shield gas	92 %Ar + 8 %CO_2
Shield gas flow rate [L/min]	16
Idle time [s]	5

$$\nabla \bullet \sigma + f = 0 \tag{2}$$

where σ denotes the stress tensor and f represents the body force vector of the model.

For the unalloyed low carbon steel, phase transformation doesn't have significant influence on the deformation and residual stress [39]. Therefore, the total strain tensor can be expressed as Equation (3):

$$\varepsilon = \varepsilon_e + \varepsilon_p + \varepsilon_t \tag{3}$$

where ε_e, ε_p, and ε_t are elastic, plastic, and thermal strain tensors respectively. The temperature dependent elastic–plastic material model is utilized, and thermal strain ε_t is calculated based on Equation (4):

$$\varepsilon_t = \int_{T_0}^{T} \alpha_t dt \tag{4}$$

where α_t is the temperature dependent thermal expansion coefficient, T is the material temperature, and T_0 is the initial temperature.

Then the stress tensor can be calculated according to Equation (5) [30]:

$$\sigma = C : \varepsilon_e \tag{5}$$

where C is the fourth-order tensor of elastic moduli. In this research, von Mises yield criterion is used for the material.

3.2. Material deposition modelling

In the WAAM process, the wire feed material is melted and deposited onto the workpiece with the movement of welding head. To simulate this material deposition, the element birth and death technique was employed. In the FE model, all elements constituting the deposited specimen were included from the beginning of the simulation.

A coupled thermal-displacement step with a very short time period of 1×10^{-10} was used to deactivate the elements constituting the deposited

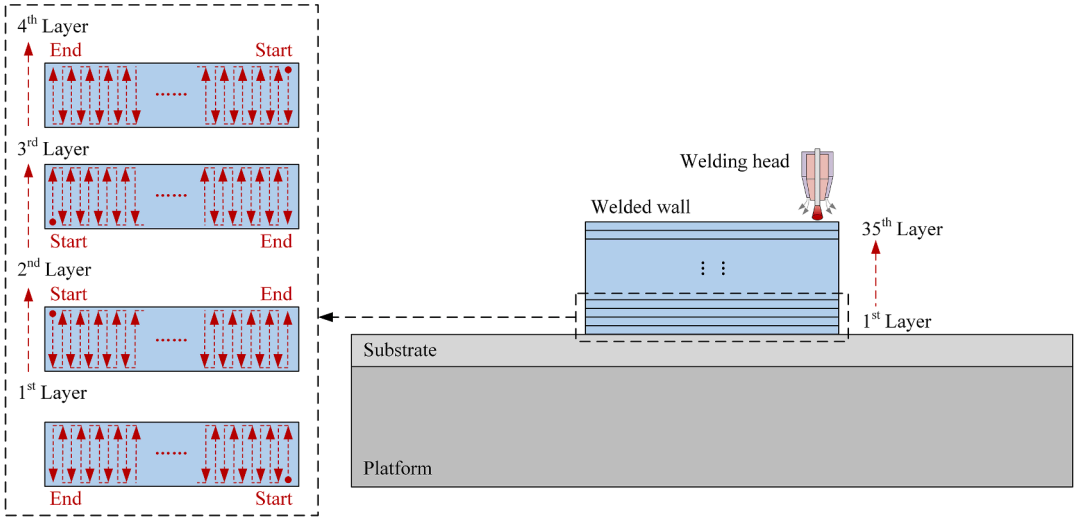

Fig. 4. Deposition trajectory of CMT process.

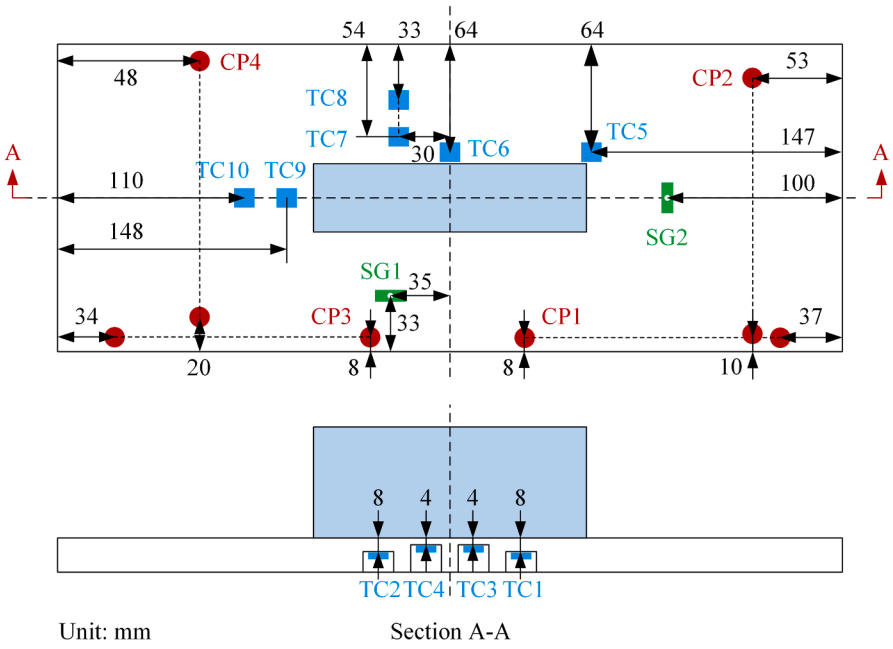

Fig. 5. Coordinates of selected positions of TCs, SGs, and CPs.

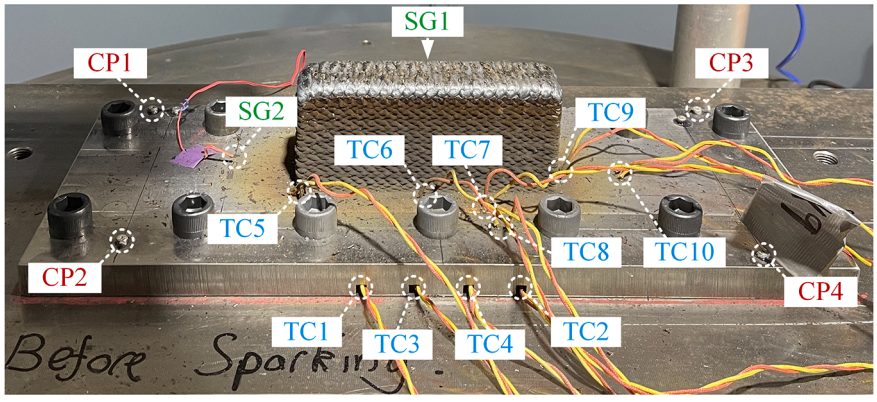

Fig. 6. Installations of TCs, SGs and CPs on the substrate.

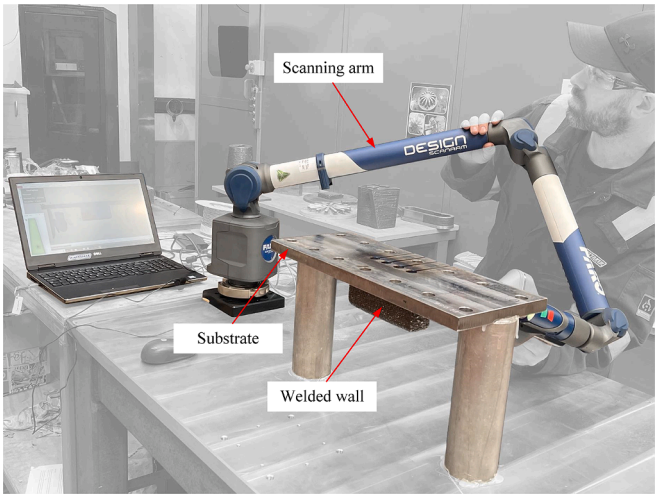

Fig. 7. Distortion measurement using the three-dimensional laser scanner.

material. Before deactivating these elements, the forces exerted by the soon-to-be-removed region on the rest of the model were stored at the boundary nodes. During the deactivation step, these forces were gradually reduced to zero, ensuring a smooth transition in the model's response. The influence of the removed region was fully eliminated by the end of the step. No further element calculations are performed for elements being removed, starting from the beginning of the step in which they are removed. These elements remained inactive until they were reactivated in later steps.

Reactivation of the inactive elements occurred step by step, following the programmed trajectory of the heat source. The schematic of element birth and death procedure is shown in Fig. 8. The elements regained their full mechanical stiffness immediately upon strain-free reactivation, with no stress, strain, and plastic strain, at the start of the step in which they are reactivated, avoiding disruption to the solution's smoothness. Thermal conductivity, however, was gradually increased from zero during the activation step to ensure solution stability. The mechanical stiffness and thermal conductivity changes of the activated elements during element activation step are illustrated in Fig. 9.

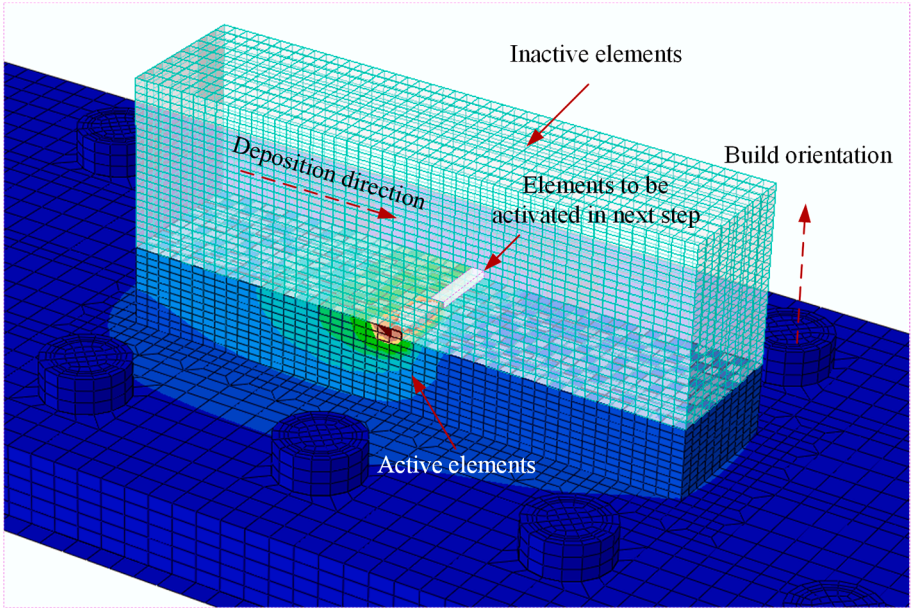

Fig. 8. Schematic of element birth and death procedure.

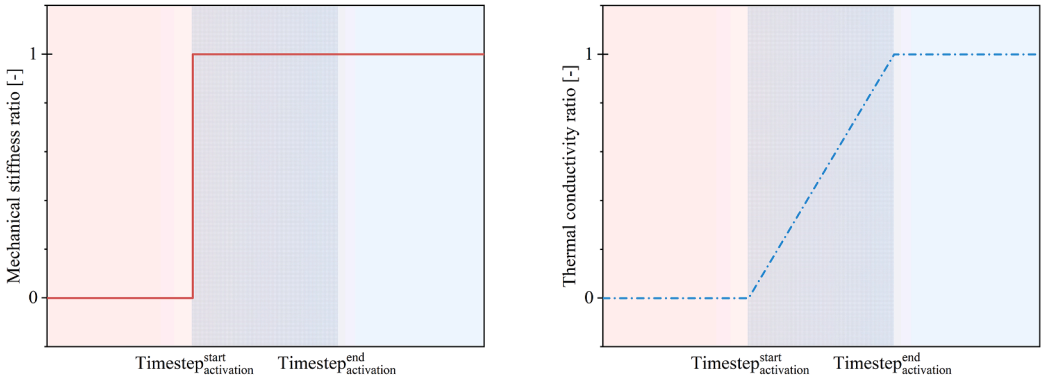

(a) Mechanical stiffness (b) Thermal conductivity

Fig. 9. Mechanical stiffness and thermal conductivity changes of the activated element during element activation step.

3.3. Acquisition of thermal physical and mechanical properties

The thermal and elastic–plastic mechanical properties of the filler material and substrate as a function of temperature are shown in Fig. 10 and Fig. 11, respectively. Thermal physical and mechanical data for WAAM filler material is currently unavailable in the literature, the

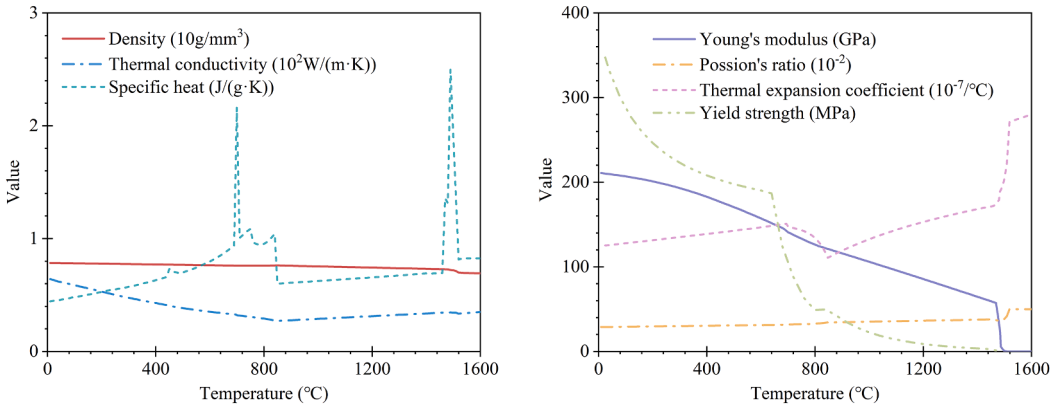

(a) Temperature-dependent physical properties (b) Temperature-dependent mechanical properties

Fig. 10. Thermal and mechanical properties of the filler material (3Dprint AM35).

thermal properties were therefore obtained through simulations based on the chemical compositions (Table 1), interested reader can refer to [40] for more information on the procedure followed herein.

3.4. Initial boundary conditions

The initial thermal condition (T_0) corresponds to a deposition process carried out at ambient temperature, see Equation (6):

$$T(x, y, z, t_0) = T_0 = 289.65\,K \tag{6}$$

Heat loss due to radiation and convection at the component's surface is considered using Equation (7):

$$q - k\frac{\partial T}{\partial \vec{n}} = \varepsilon\sigma(T - T_0)^4 + h(T - T_0) \tag{7}$$

where q is the surface heat flux, $\vec{n}$ is a unit vector normal to the boundary surface, ε is the grey body radiation coefficient taken as 0.73, σ is Stefan-Boltzmann constant with its value being $5.6704 \times 10^{-8}\,W/(m^2K^4)$, h is heat convection coefficient which is set as $20\,W/(m^2K)$ and T is the temperature at the surface nodes [41]. Note that the heat exchange coefficient of the bottom surface of the substrate is set to $300\,W/(m^2K)$ to simulate cooling through the platform [18].

The geometry of the model and its coordinates are schematically illustrated in Fig. 12. The FE model comprises four parts: welded specimen, bolts, substrate, and platform. The edges of the platform's bottom surface were pinned. The bottom surfaces of the bolts were merged with the top surface of the platform to simulate a bolted connection. The surfaces interactions between substrate and bolt, and substrate and platform, were defined as surface-to-surface contact with hard contact along the normal direction and tangential friction coefficient of 0.3. The bolt pretension force was set to 10.2 kN.

3.5. Heat source model

To simulate the heat input of CMT process, the Goldak's double ellipsoidal heat source model was adopted [42]. The heat input was divided into front and rear ellipsoids, whose shapes are determined by individual parameters. The schematic of the Goldak's double ellipsoidal heat source is shown in Fig. 13. The heat flux in the coordinates systems (x, y, z, t) can be described with Equations (8) to (10):

$$Q_{front}(x, y, z, t) = \frac{6\sqrt{3}f_{front}\eta P}{a_{front}bc\pi\sqrt{\pi}}\exp\left(-\frac{3(x - vt)^2}{a_{front}^2} - \frac{3y^2}{b^2} - \frac{3z^2}{c^2}\right) \tag{8}$$

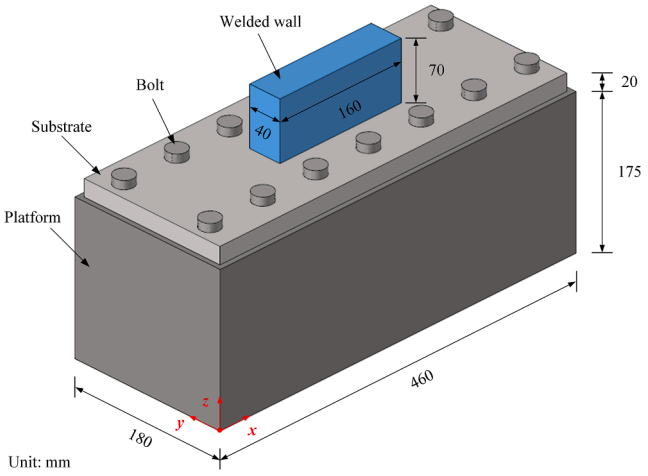

Fig. 12. Geometry and coordinates of the model.

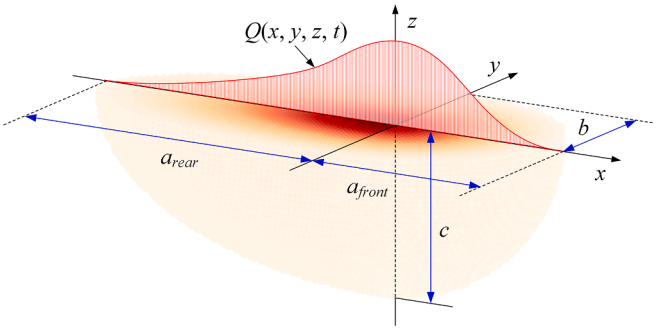

Fig. 13. Schematic of Goldak's double ellipsoidal heat source.

$$Q_{rear}(x, y, z, t) = \frac{6\sqrt{3}f_{rear}\eta P}{a_{rear}bc\pi\sqrt{\pi}}\exp\left(-\frac{3(x - vt)^2}{a_{rear}^2} - \frac{3y^2}{b^2} - \frac{3z^2}{c^2}\right) \tag{9}$$

$$f_{front} + f_{rear} = 2 \tag{10}$$

where P is the average power, η is the heat source efficiency which is taken equal to 0.9 in the experimental system [41], f_{front} and f_{rear} are the welding power fraction introduced to front and rear ellipsoids respectively, a_{front} (front ellipsoidal length), a_{rear} (rear ellipsoidal length), b (ellipsoidal width), and c (ellipsoidal depth) are the parameters that

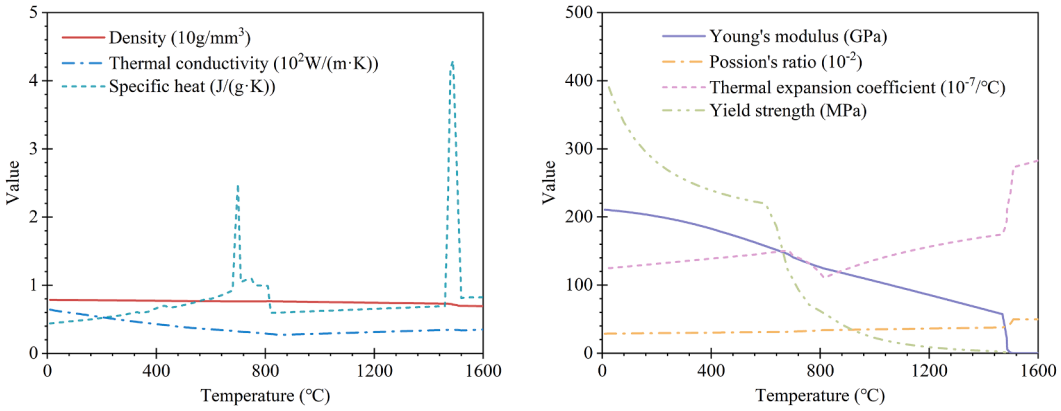

(a) Temperature-dependent physical properties

(b) Temperature-dependent mechanical properties

Fig. 11. Thermal and mechanical properties of the substrate (S355).

determine the shape of the melting pool, v is the travel speed, and t is the time.

To ensure modelling accuracy, the double ellipsoidal heat source parameters were calibrated using experimental data from a single-pass welding test conducted with the same CMT process parameters as listed in Table 3. Fig. 14 compares the simulated cross-sectional geometry of the weld with the experimental bead-on-plate profile. While the heat source model does not precisely capture the fusion line shape due to the limitations of the double ellipsoidal heat source model's smooth geometry and the omission of melting pool flow in the FE model, the resulting heat affected closely matches the experimental observations. This similarity suggests that the chosen heat source parameters are adequate for simulating thermal behaviour. The specific parameter values used for the double ellipsoidal heat source are provided in Table 4. This approach to qualitatively verify heat source parameters is also reported in the literature [26,43]. Quantifying the uncertainty in the FE simulation introduced by these heat source parameters will be studied in future research.

3.6. Convergence analysis

Mesh convergence study assessed FE model accuracy, based on thermal cycles and stress development. FE meshes with element sizes of 1 mm, 2 mm and 3 mm were generated (see Fig. 15). TC1 thermal cycles and SG1 stress development (S11) were selected as baseline, and the simulation results for the 3 different mesh sizes were compared, as depicted in Fig. 16(a) and Fig. 16(b) respectively. Simulation results of all models accurately capture the experimental measurements. TC1′s first measured peak temperature was 173.2 °C, giving a relative simulation error of 6.3 %, 7.7 %, and 10.7 % respectively for mesh of sizes of 1 mm, 2 mm and 3 mm. The first peak of SG1 measurement was 117.6 MPa, giving a simulation deviation of 7.0 %, 16.2 %, and 21.3 % respectively. While 1 mm mesh excels in accuracy, it incurs a twelve-fold increase in computational time compared to 3 mm mesh, with insignificant simulation difference. Thus, to balance simulation accuracy and computational burden, a 3 mm mesh was selected.

During the FE simulations, another key parameter to avoid convergence issues is the solver technique used to calculate the thermal-displacement equations. Two types of solvers are available in ABAQUS 2020, "fully coupled analysis" and "separated analysis". Both exhibit similar thermal and stress fields for WAAM simulations. However, fully coupled analysis converges more easily while being generally more time consuming, compared to the separated analysis. Alternatively, as the simulation proceeds, the stress evolution from the separated analysis may occasionally oscillate, implying instability of the solution.

Table 4
Parameter values of double ellipsoidal heat source.

Parameter	a_{front} [mm]	a_{rear} [mm]	b[mm]	c[mm]	f_{front}	f_{rear}
Value	3.0	6.0	2.5	3.0	0.6	1.4

Meanwhile, the difference in computational efficiency between the two solvers gradually decreases as the simulation proceeds. In this research, convergence was favoured, and a fully coupled analysis was adopted. Fixed time increment can accelerate computations slightly. However, it can be detrimental to convergence which is why automatic time increment was presently used and was in the range of "$1 \times 10^{-6} \sim 0.1$" seconds.

4. Comparison between FE model and experiment

As detailed in Section 3, the validated approach utilized a fully coupled (FC) three-dimensional thermal–mechanical model, where thermal and stress equations are solved synchronously. The number of finite elements is 40,500. Solid C3D8T elements were used to model the welded specimen, the bolts, and the substrate, while the platform was meshed with shell S4RT elements to optimize computational efficiency. A sensitivity assessment was performed to assess the impact of various factors, including ambient temperature, element activation strategies, alignment errors of thermocouples and strain gauges, and the use of a sequentially coupled approach, on the simulation accuracy of the FE model.

4.1. Fully coupled thermal-stress analysis

4.1.1. Temperature field

The evolution of the temperature field during the CMT process is shown in Fig. 17, divided into four rows for different deposition layers, i.e., 10th layer, 20th layer, 30th layer and 35th layer, corresponding to deposition times of $t_1 = 1859.4$ s, $t_2 = 3814.9$ s, $t_3 = 5770.4$ s and $t_4 = 6744.0$ s. The left column gives the FE modelled temperature field, and the right column gives the measured temperature field from thermography camera. The white lines in Fig. 17 are isotherms, with indication of their corresponding temperatures. FE model isotherms are consistent with those obtained in the thermography pictures, indicating accurate thermal field evolution prediction of the FE model. The grey area in the FE model represents the melting pool region, with a temperature higher than 1500 °C. The distances between successive isotherms reveal higher temperature gradient in the front deposition direction of the deposition than in the rear one. Moreover, the temperature of the specimen

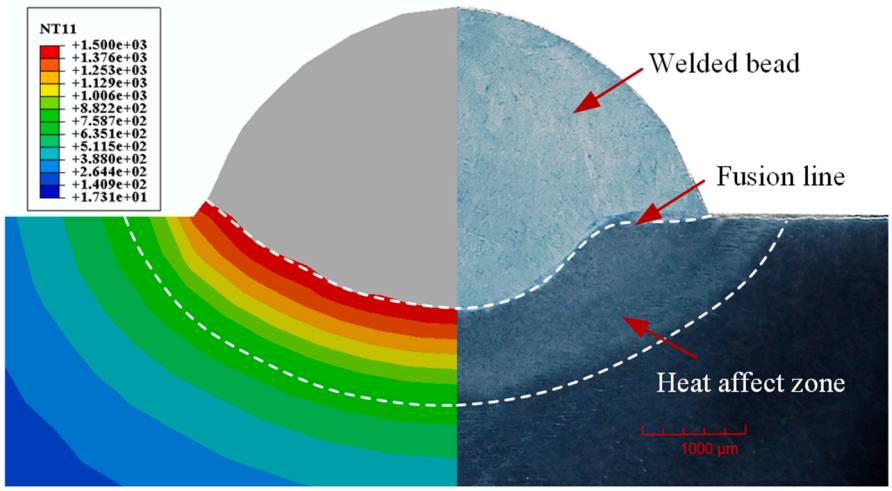

Fig. 14. Comparison of simulated thermal profile and experimental bead-on-plate cross-section.

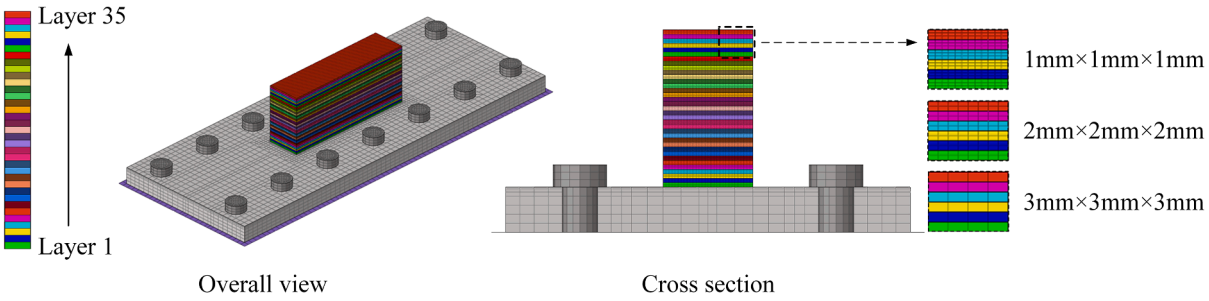

Fig. 15. FE models with different mesh sizes.

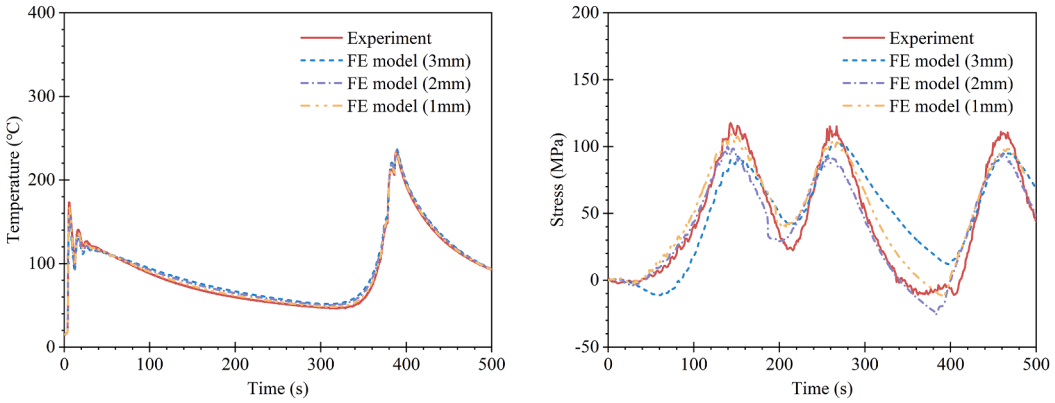

(a) Thermal cycles of TC5 (b) Stress evoultions of SG1

Fig. 16. Comparison of thermal cycles and stress evolutions with different mesh sizes, up to 500 s.

increases with the deposition height due to heat accumulation, which is also consistent with what is reported in the literature for various metals [38,41]. The temperature of previously deposited layer rises from 150 ~ 250 °C to 375 ~ 500 °C as the deposition height increases, and the area covered by the same isotherm increases. In the early stages of deposition, the cooling of the specimen is dominated by heat transfer between the welded specimen, substrate, and platform. With higher deposits however, surface radiation and air convection become the primary heat loss modes. Therefore, to avoid extreme heat accumulation, it is important to employ effective welding trajectory and interlayer temperature control strategies to prevent overheating.

To further illustrate the proposed FE model precision, the thermal cycles measured with thermocouples TC1 to TC10 are compared against the simulation results, see Fig. 18 (locations of TCs provided in Fig. 5). The thermocouples are categorised based on their locations: embedded in the substrate (TC1 ~ TC4), along the fusion line of the welded specimen (TC5 and TC6), along the transverse direction (TC7 and TC8) and along the longitude centreline (TC9 and TC10). Bilinear interpolation method is used to calculate the temperature, considering the four adjacent nodes in the same plane using Equation (11):

$$T_{(x,y,t)} = \frac{1}{(x_2-x_1)(y_2-y_1)}\begin{bmatrix} x_2-x & x-x_1 \end{bmatrix}\begin{bmatrix} T_{(x_1,y_1,t)} & T_{(x_1,y_2,t)} \\ T_{(x_2,y_1,t)} & T_{(x_2,y_2,t)} \end{bmatrix}\begin{bmatrix} y_2-y \\ y-y_1 \end{bmatrix} \tag{11}$$

where $T_{(x,y,t)}$ is the temperature to be predicted at coordinate (x, y) at time t. $T_{(x_1,y_1,t)}$, $T_{(x_1,y_2,t)}$, $T_{(x_2,y_1,t)}$, and $T_{(x_2,y_2,t)}$ are the simulated temperatures at the neighbouring nodes in the FE model.

The simulated thermal cycles closely match the measured data, the trend repeating periodically during the deposition process due to the cyclical motion of the welding heat source. For the embedded thermocouples (TC1 ~ TC4), the peak temperatures of TC3 and TC4 are 867.9 °C and 910.6 °C respectively, higher than TC1 (500.6 °C) and TC2 (542.5 °C), due to proximity to the deposition surface (4 mm versus 8 mm). Accuracy of the peak temperature predictions of TC1 ~ TC4 diminished slightly when the welding head was positioned right on top of the thermocouples. In the experiment, it was observed that the drilled holes for thermocouples installation were partially melted due to extreme high temperature of liquid metal, which contributed to the higher measured peak temperatures. In terms of TC5 and TC6, TC6 exhibits more stable temperature, as it is centrally located within the substrate, and TC5, located at a corner of the cuboid specimen, exhibits large fluctuations. The trends of thermal cycles provided by TC7 and TC8 are in good agreement, with TC7's higher peak temperature attributed to its proximity to the fusion line (10 mm versus 31 mm). TC8's higher prediction error could be linked to installation inaccuracies of thermocouple pins, which were installed with a relatively large distance between the pins, see Fig. 6. TC9 is closer to the welded specimen, so it shows higher temperature values compared to TC10. The crest of TC10 grows with time during deposition, indicating temperature rise at the far end of the substrate due to heat accumulation which the model does not capture well.

Meanwhile, the comparison of experimentally measured (Expt.) and FE simulated thermal cycles of TC1 to TC10 at four specific time frames of t_1 = 1859.4 s, t_2 = 3814.9 s, t_3 = 5770.4 s and t_4 = 6744.0 s are summarised in Table 5, along with the relative simulation errors (REs). The time frames of t_1 ~ t_4 are marked in Fig. 18. It can be observed that the REs at the t_1 time frame is relatively low, with the highest RE at TC5 of 26.9 %, and the lowest RE at TC10 of 9.4 %. As the deposition process progresses, the simulation discrepancies accumulate, resulting in an increase in RE values. At t_4 time frame, RE values have risen to a range of 23.0 % to 40.8 %.

Overall, the FE model can simulate the trends and values of the temperature cycles quite precisely. Particularly, it can accurately capture every fluctuation in the thermal cycles. The main difference appears

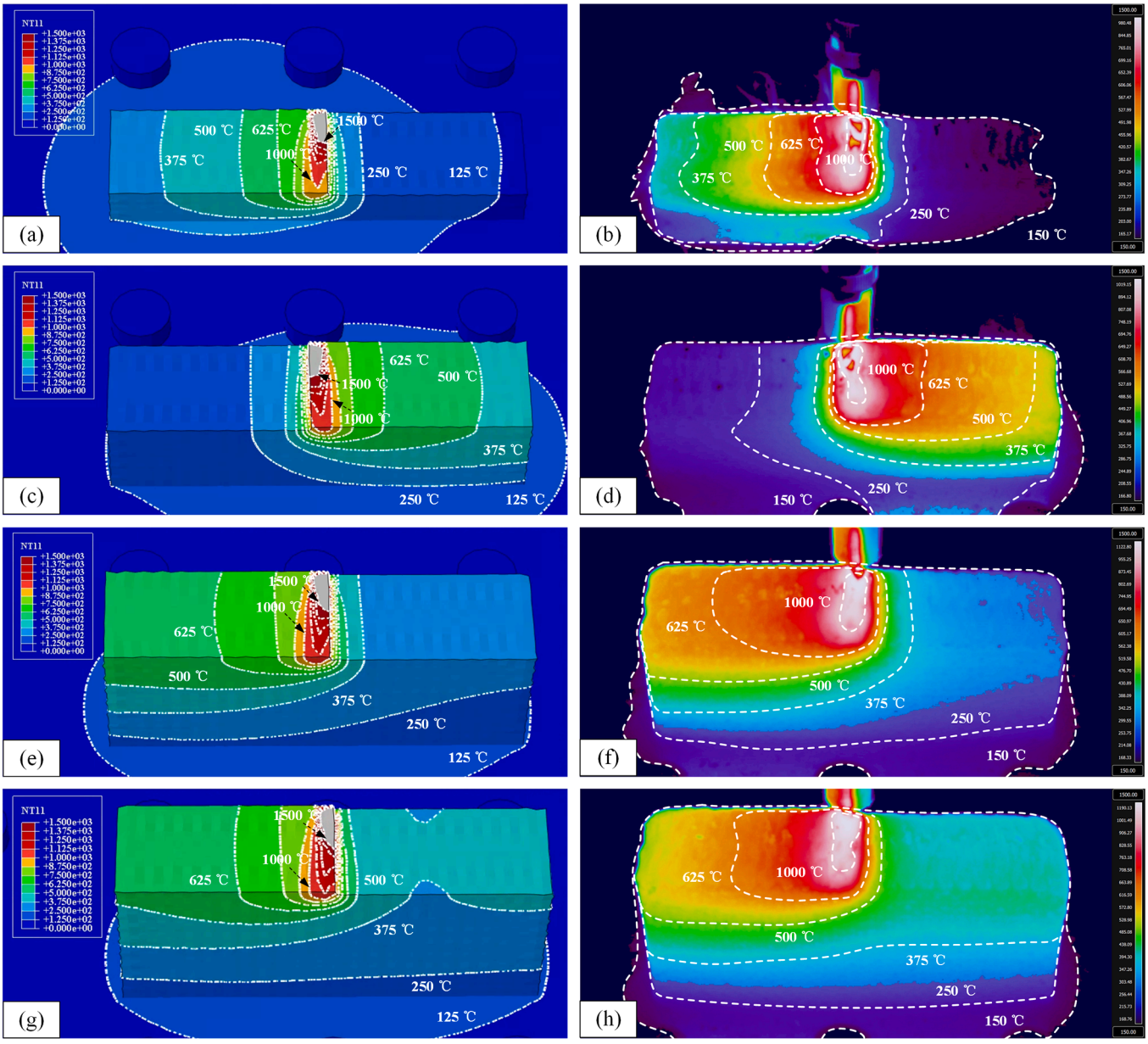

Fig. 17. Evolution of temperature fields in FE model (left column) and experimental measurements (right column): (a, b) 10th layer ($t_1 = 1859.4$ s); (c, d) 20th layer ($t_2 = 3814.9$ s); (e, f) 30th layer ($t_3 = 5770.4$ s); and (g, h) 35th layer ($t_4 = 6744.0$ s).

to be related to how well heat builds up and it could be attributed to the following reasons. Firstly, the alignment errors of K-type thermocouples installation which were welded to the substrate by spot welding and the distance between the two pins of K-type thermocouples can introduce measurement errors. Secondly, depositing one specimen takes approximately two hours during which, through heat convection and radiation, we noted an increase in ambient temperature from 15.7 °C to 17.9 °C after the experiment. Ambient temperature offset changed the thermal boundary conditions and introduced simulation error. However, quantifying the coupled thermal interactions between the atmosphere and the specimen is rather complex, and beyond the scope of this study. Therefore, in this FE model, a constant ambient temperature of 16.5 °C was adopted.

4.1.2. Stress and deformation fields

Fig. 19 displays the deformation and stress fields of the specimen at different deposition stages. The rows correspond to the different deposition layers, i.e., 10th layer, 20th layer, 30th layer and 35th layer, from top to bottom, corresponding to deposition times of $t_1 = 1859.4$ s, $t_2 = 3814.9$ s, $t_3 = 5770.4$ s and $t_4 = 6744.0$ s, respectively. The left column shows the vertical deformation (U3) field, while the right column portrays the von Mises stress field.

The maximum vertical deformation appears in the edge area of the transverse centreline of the substrate, indicated by the dashed black line area in the left column of Fig. 19. As the deposition layers increase, the maximum deformation values rise from 0.509 mm to 0.522 mm, indicating that higher deposition leads to greater deflection.

In terms of stress distribution, the right column of Fig. 19 shows that the maximum stress is concentrated in the connection area between the substrate and the welded specimen (also marked by the dashed black line area). The maximum stress shifts between the left and right sides of the connection area with changing of deposition direction. This shift is due to the unbalanced heat input in the deposited wall during the deposition process, as previously reported in [34]. The schematic of stress evolution within the high stress region (dashed black line area) for the first three layers are shown in Fig. 20. The blue area represents the

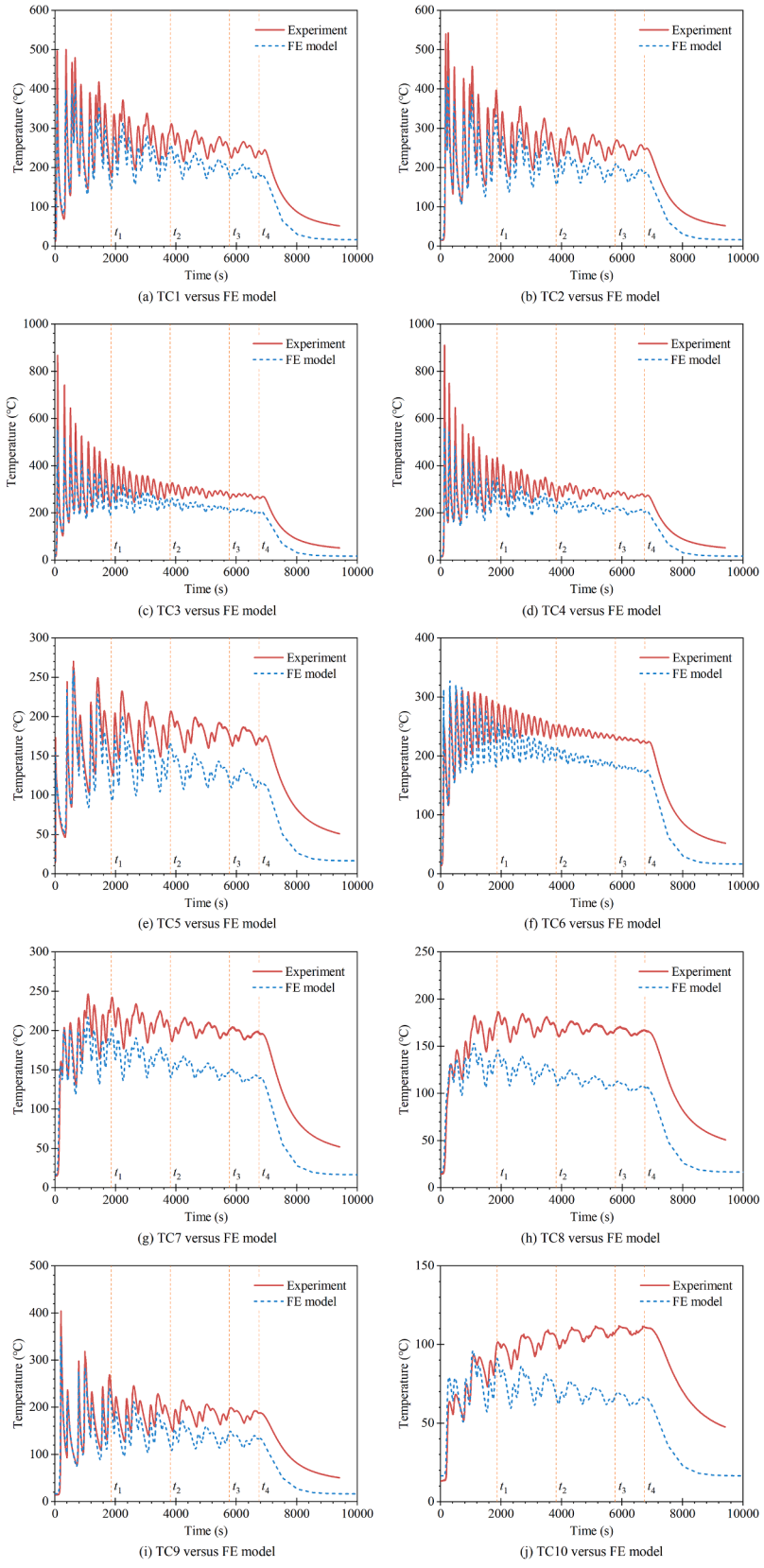

Fig. 18. Thermal cycles comparison between experimental measurements (solid line) and simulation results (dash line).

Table 5
Comparison of the measured and FE simulated temperatures at different time frames.

		TC1	TC2	TC3	TC4	TC5	TC6	TC7	TC8	TC9	TC10
t_1	Expt. [°C]	176.5	378.6	252.1	423.5	134.3	238.2	238.8	182.4	236.1	100.4
	FE [°C]	145.6	312.9	226.4	348.2	98.2	212.5	199.7	143.7	208.6	91.0
	RE [%]	17.5	17.4	10.2	17.8	26.9	10.8	16.4	21.2	11.7	9.4
t_2	Expt. [°C]	302.6	217.5	285.8	253.2	205.6	233.3	194.7	167.7	166.6	104.4
	FE [°C]	255.5	160.3	244.0	194.7	165.3	196.4	141.7	112.7	116.8	67.8
	RE [%]	15.6	26.3	14.6	23.1	19.6	15.8	27.2	32.8	29.9	35.1
t_3	Expt. [°C]	238.2	263.2	266.6	280.8	175.1	229.2	200.8	166.9	195.3	107.6
	FE [°C]	177.8	207.2	202.7	219.2	117.2	177.6	147.5	110.9	147.5	67.2
	RE [%]	25.3	21.3	24.0	21.9	33.0	22.5	26.5	33.6	24.5	37.6
t_4	Expt. [°C]	242.4	245.8	265.3	269.3	172.3	223.9	196.8	166.4	187.8	111.1
	FE [°C]	183.5	185.7	200.7	203.2	118.6	172.3	139.2	106.4	133.5	65.8
	RE [%]	24.3	24.5	24.3	24.5	31.2	23.0	29.2	36.1	28.9	40.8

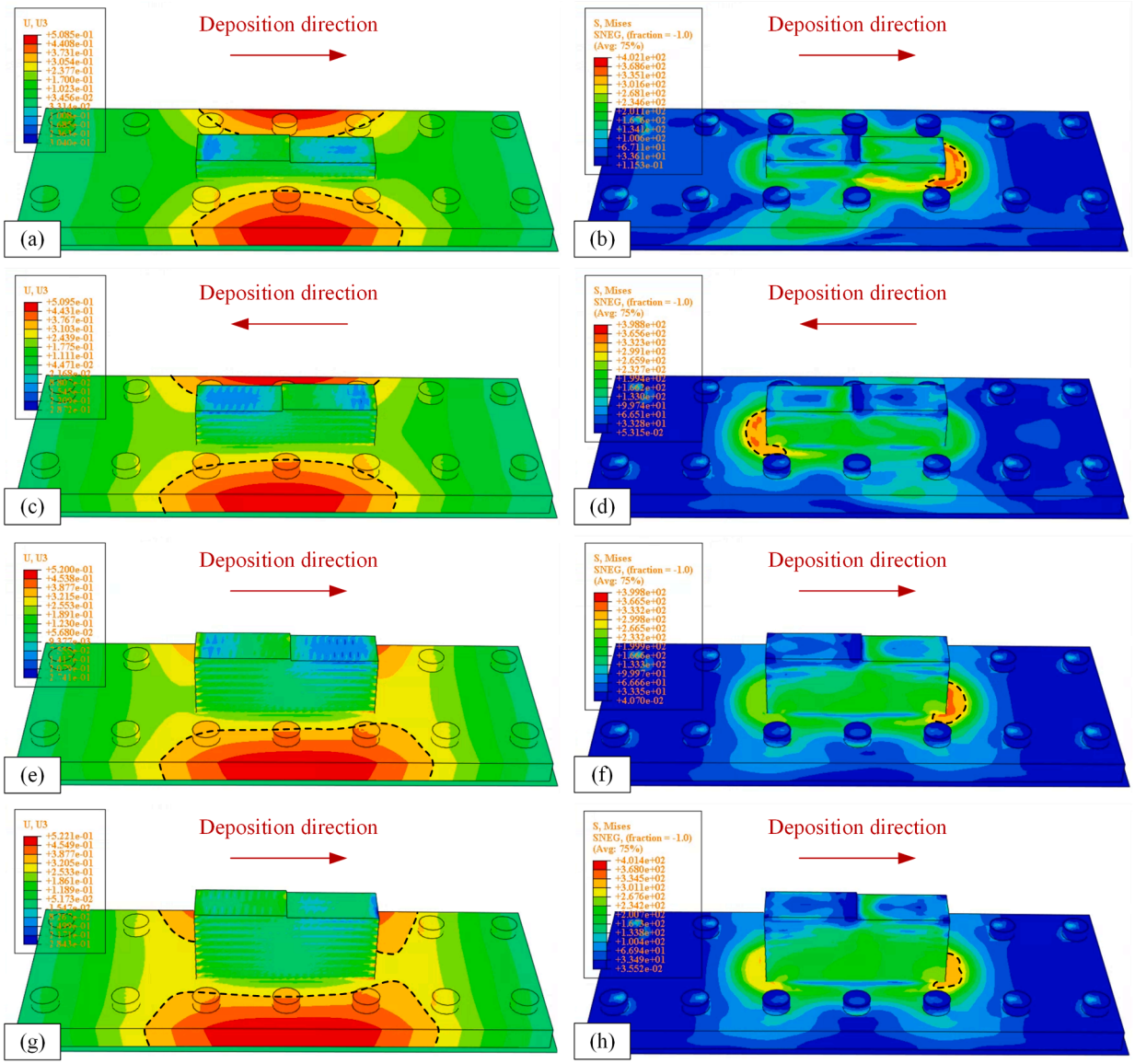

Fig. 19. Simulated vertical deformation (left column) and von Mises stresses (right column) for different deposition layers: (a, b) 10th layer (t_1 = 1859.4 s); (c, d) 20th layer (t_2 = 3814.9 s); (e, f) 30th layer (t_3 = 5770.4 s); and (g, h) 35th layer (t_4 = 6744.0 s).

relationship between temperature and substrate's yield strength, where the dashed lines trace the stress evolution during deposition. The stress development can be divided into three stages: (i) Elastic compression: as the temperature rises, compressive stress builds up elastically until it surpasses the compressive yield stress; (ii) Stress relaxation: the compressive stress decreases as the heat source moves away; and (iii) Plastic tension: upon cooling, the material first experiences a brief stage of elastic tensile stress, followed by plastic tensile stress. These observations align with previous studies [30,31,34]. After the substrate's temperature stabilizes, the local maximum tensile von Mises stress

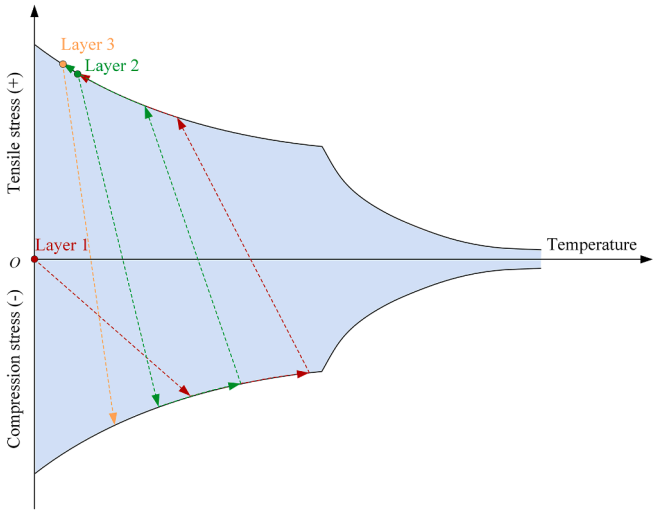

Fig. 20. Schematic of stress evolution within the high stress region within the connection area between the substrate and welded specimen.

reaches the yield strength of the substrate, approximately 400 MPa. The observed stress stability is typical for WAAM processes where heat input is well-managed, and the mechanical constraints remain constant.

The measured stress cycles at SGs (longitudinal stress S11 for SG1 and transverse stress S22 for SG2) were compared against the FE results, see Fig. 21. Three distinct stages are identified from the transient stress evolution: deposition (pink region), cooling (shadow region), and unclamping (cyan region). During deposition, the localized heating induces thermal expansion in the newly deposited material, leading to transient tensile stresses in the region near the weld and compressive stresses in surrounding areas due to constraints imposed by the substrate and previous layers. The thermal stresses oscillated cyclically with the temperature cycles, the rate being governed by the welding path and procedure. With elevated deposition height, the systematic stiffness increases, leading to the stress magnitude slightly decreasing. As the material cools during cooling stage, contraction occurs, which increases tensile stress in the deposited material while causing compressive stress in the substrate due to the mismatch in thermal contraction rates. This is expected behaviour as thermal gradients generate internal stresses, especially at the interface between the substrate and the welded material. The sharp stress changes during unclamping are due to the release of external mechanical constraints (bolts), which had previously restricted the deformation of both the substrate and the deposited material. The component undergoes springback, causing the redistribution of residual stresses. Additionally, the bolted connections create localized stress concentrations that are alleviated upon unclamping, which explains the sharp stress drops near the bolt locations.

Table 6 compares the experimentally measured and FE simulated stresses at five specific time frames of $t_1 = 1859.4$ s, $t_2 = 3814.9$ s, $t_3 = 5770.4$ s, $t_4 = 6744.0$ s and $t_5 = 11300$ s. At t_1, the RE at SG1 is 19.4 %, and at SG2 is 34.1 %. As the deposition process progresses, RE values increase significantly, reaching 106.8 % at SG1 and 67.0 % at SG2 by the t_4 time frame. The maximum measured transient stresses at SG1 and SG2 are 117.6 MPa and 67.2 MPa respectively, with corresponding simulation values of 117.6 MPa and 59.5 MPa, resulting in REs of 8.8 % and 11.5 %. After unclamping at t_5, the simulated transient stresses at SG1 and SG2 are minimized, with simulated values of −139.1 MPa and −133.2 MPa, and the RE at SG1 is 432.4 % and the RE at SG2 is 8.4 %.

Based on the comparison, it can be concluded that the proposed FE model effectively captures the stress evolution across all three phases of the WAAM process. The discrepancies between experimental measurements and simulation results can be attributed to the following factors in addition to common testing inaccuracies. Firstly, the exact locations of the SGs do not precisely correspond to the integration points in the FE model. Although bilinear interpolation was used to approximate these values, some interpolation errors are inevitable. Secondly, due to the high thermal impact during deposition, measurement errors caused by thermal expansion were unavoidable, although thermal compensation was considered. Additionally, simplifications, such as uniform bolt pretension forces and idealized contact conditions between the substrate and bolts, could affect the exact magnitude of the stress redistribution but not the overall trend. Finally, while the simulated stress evolution at SG1 aligns closely with experimental measurements during the initial 1500 s (red solid line), it begins to diverge as the deposition proceeds

Table 6
Comparison of the measured and FE simulated stresses at different time frames.

		SG1	SG2
t_1	EXP. [MPa]	85.7	−110.3
	FE [MPa]	69.1	−72.7
	RE [%]	19.4	34.1
t_2	EXP. [MPa]	52.8	−48.5
	FE [MPa]	−9.1	−23.9
	RE [%]	117.3	50.8
t_3	EXP. [MPa]	66.2	−55.4
	FE [MPa]	8.2	−25.1
	RE [%]	87.6	54.7
t_4	EXP. [MPa]	66.9	−44.5
	FE [MPa]	−4.5	−14.7
	RE [%]	106.8	67.0
t_5	EXP. [MPa]	41.8	−144.0
	FE [MPa]	−139.1	−133.2
	RE [%]	432.4	7.5

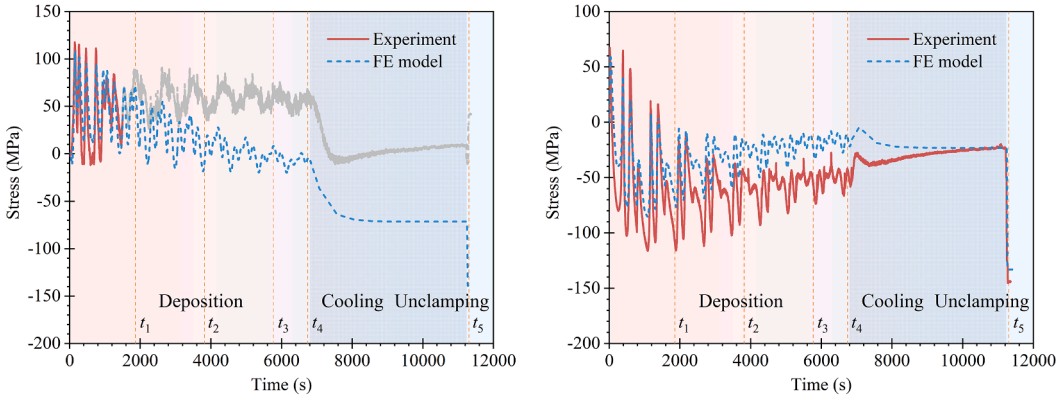

(a) Stress evolutions of SG1

(b) Stress evolutions of SG2

Fig. 21. Transient stress comparison between experimental measurements (solid line) and simulation results (dash line).

(1500 ~ 12000 s, grey solid line). This divergence is partly attributed to the high temperatures at SG1, which caused it to loosen from the substrate due to failure of the glue. The SG1 was found detached after the experiment, and the problem was also observed in other trials. This detachment is also corroborated by the increased noise in measured stress data after 1500 s.

To address the differences between measured and simulated stress cycles, several strategies could be adopted in future experiments to improve measurement accuracy: (i) Precise installation of SGs: SGs should be installed at exact, predefined locations to minimize alignment errors. Ensuring accurate placement will reduce interpolation errors and improve correlation with FE model. (ii) Consider temperature exposure: The installation locations for SGs should be carefully selected based on anticipated temperature exposure. By avoiding areas with extreme heat during deposition, adhesive failure of the SGs can be prevented. (iii) Use array sensors: Instead of relying on a few individual SGs, an array of sensors could be used to capture a more comprehensive picture of stress evolution across the component. This approach would provide a better understanding of stress distribution and improve the robustness of experimental data.

4.2. Sensitivity assessment

4.2.1. Ambient temperature offset

As described in Section 4.1.1, the ambient temperature was switched from 15.7 °C to 17.9 °C during the experiment. To assess the impact of the temperature offset on potential simulation uncertainties, FE simulations were performed for the first 500 s applying ambient temperature (AT) boundary conditions of 15.7 °C and 17.9 °C respectively. The simulated temperature cycles of TC5 with different ATs are shown in Fig. 22.

The highest measured temperature is 232.9 °C at 387.5 s, and the corresponding simulated temperatures with ATs of 15.7 °C, 16.5 °C and 17.9 °C are 234.4 °C, 234.9 °C and 235.9 °C respectively, yielding simulation errors of 0.626 %, 0.859 % and 1.291 %. The difference in simulated temperatures between the ATs of 15.7 °C and 17.9 °C is 1.5 °C, resulting in a simulation error difference of 0.665 %. Within the first 500 s, the impact of ATs on thermal stress is almost negligible, as variations in temperature fields and mechanical boundaries are not yet significant during the early deposition stage. As the deposition continues, heat divergences in the workpiece lead to variations in stress evolution and distribution, which are sensitive to the progression of thermal cycles.

4.2.2. Element activation strategies

The element death and birth technique is used to model the material deposition process. As illustrate in Fig. 8, the long pass of the zigzag trajectory is divided into two simulation steps in the FE model, i.e., half-pass activation strategy. To assess the sensitivity of the FE model to different element activation strategies, two additional element activation strategies of pass-by-pass activation and layer-by-layer activation were evaluated. The schematics of pass-by-pass and layer-by-layer element activation strategies are shown in Fig. 23. In the pass-by-pass activation strategy, the entire long pass of the zigzag trajectory is activated within a single step. In contrast, the layer-by-layer activation strategy activates all elements within the same deposition layer at once.

The simulated thermal cycles of TC5 and the stress evolutions of SG1 for different activation strategies are presented in Fig. 24. The simulated highest temperatures for the half-pass, pass-by-pass, and layer-by-layer strategies are 234.9 °C, 238.1 °C and 248.5 °C respectively, resulting in simulation errors of 0.859 %, 2.233 % and 6.278 %. Similarly, the experimentally measured local maximum stress of SG1 at 467.0 s is 110.5 MPa, while the simulation results for the half-pass, pass-by-pass, and layer-by-layer strategies are 95.0 MPa, 104.1 MPa and 98.4 MPa, yielding simulation errors of 14.027 %, 5.792 % and 10.950 % respectively. It's also noticed that the half-pass activation strategy has the highest simulation accuracy for the local minimum stresses.

The choice of element activation strategies affects the thermal and mechanical boundary conditions of the FE model. While the pass-by-pass and layer-by-layer strategies simplify the simulation by reducing the number of simulation steps, care must be taken to select an appropriate strategy that accurately represents the real material deposition process. Inappropriate activation strategies can create unrealistic boundary conditions, and these simulation inaccuracies may accumulate as the simulation progresses.

4.2.3. Alignment errors of thermocouples and strain gauges

Misalignments in the installation of thermocouples and strain gauges can introduce measurement inaccuracies in temperature and strain measurements, impacting the reliability of experimental data. To investigate the influence of alignment errors, the positioning of TC5 and SG1 was analysed, whose positions within FE model are schematically shown in Fig. 25. Simulation results from nodes adjacent to TC5 and SG1 were extracted to quantify potential measurement errors. Nodes P1 ~ P4 are adjacent to TC5, and nodes Q1 ~ Q4 are adjacent to SG1, representing the deviations along directions of V1 ~ V4. Specifically, P1 and Q1 deviate transversely towards the deposited wall, while P2 and Q2 deviate away from the deposited wall. P3, P4, Q3, and Q4 indicate longitudinal deviations. The distances between TC5 and P1 ~ P4 are 3.5 mm, and the distances between SG1 and Q1 ~ Q4 are 7.0 mm.

The thermal cycles at TC5 and adjacent nodes are summarised in Fig. 26(a), and the thermal gradients in the V1 ~ V4 directions are shown in Fig. 26(b). It was observed that small misalignment in TC5 positioning could lead to considerable discrepancies in recorded

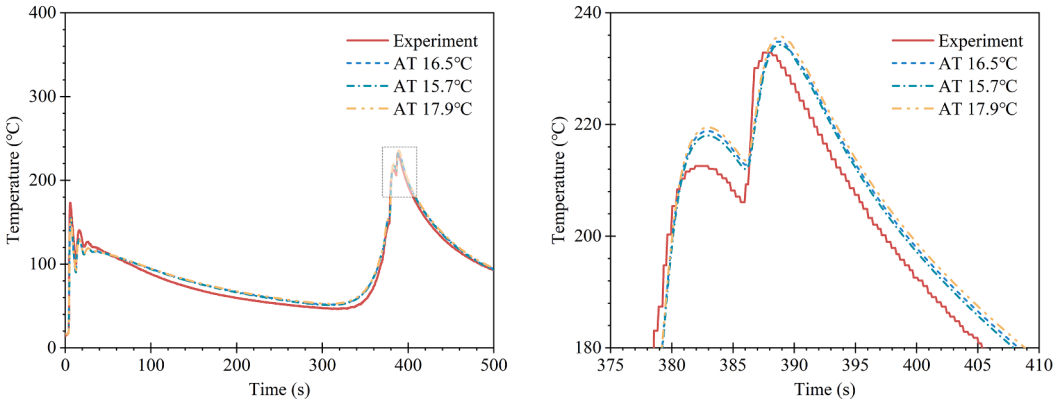

(a) Thermal cycles of TC5

(b) Enlarged view of the thermal cycle

Fig. 22. Simulated thermal cycles with different ambient temperature boundary conditions, up to 500 s.

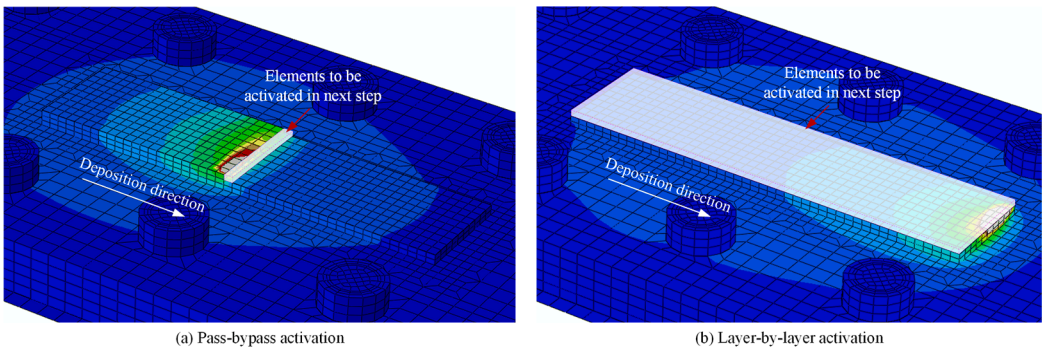

(a) Pass-by-pass activation (b) Layer-by-layer activation

Fig. 23. Schematics of pass-by-pass and layer-by-layer element activation strategies.

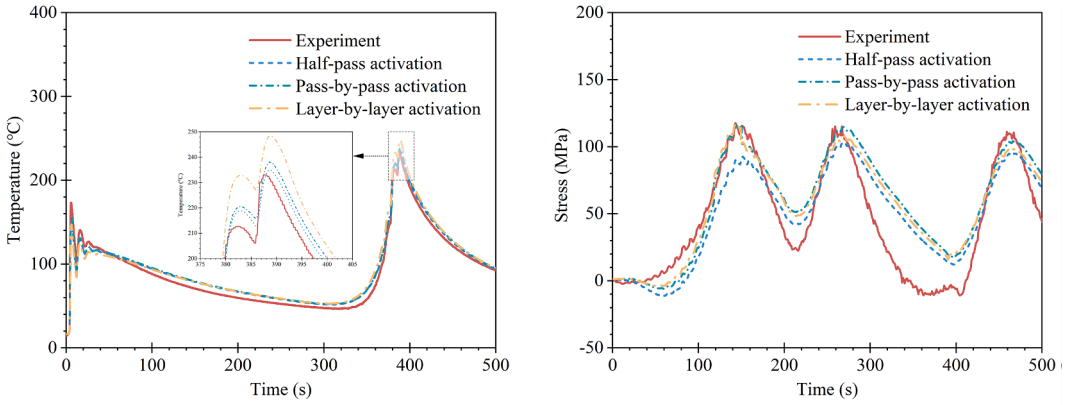

(a) Thermal cycles of TC5 (b) Stress evolutions of SG1

Fig. 24. Simulated thermal cycles and stress evolutions with different element activation strategies, up to 500 s.

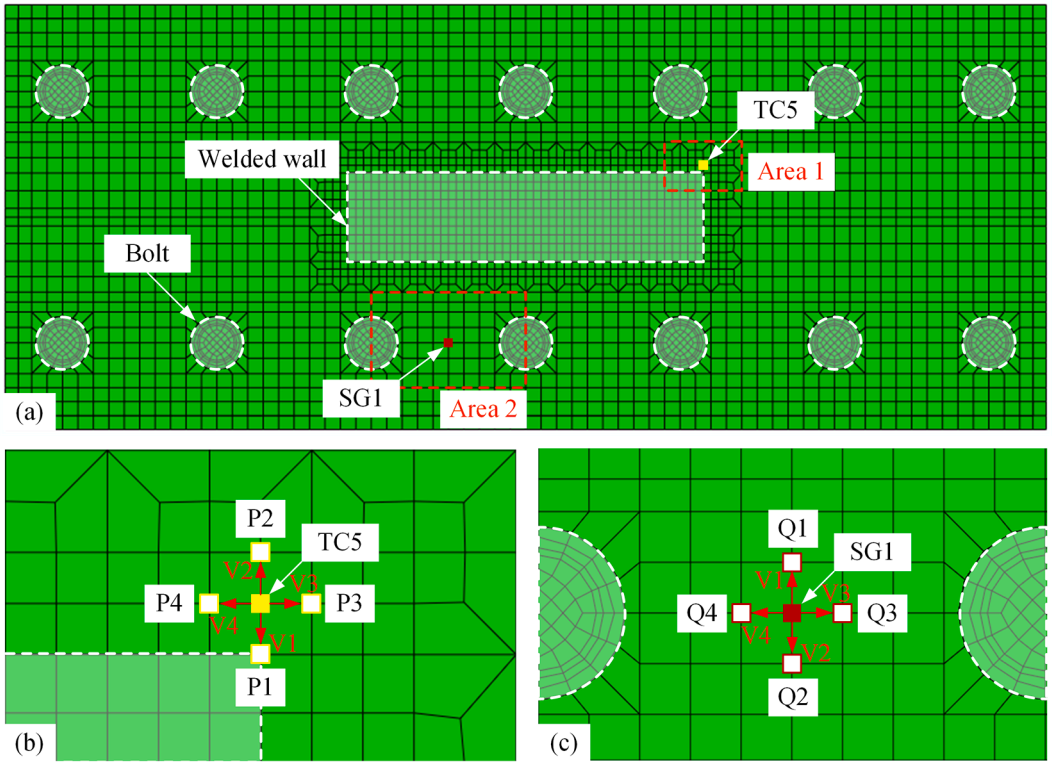

Fig. 25. Schematics of the thermocouples and strain gauges alignment errors: (a) Top view of FE mesh; (b) An enlarged view of Area 1; and (c) An enlarged view of Area 2.

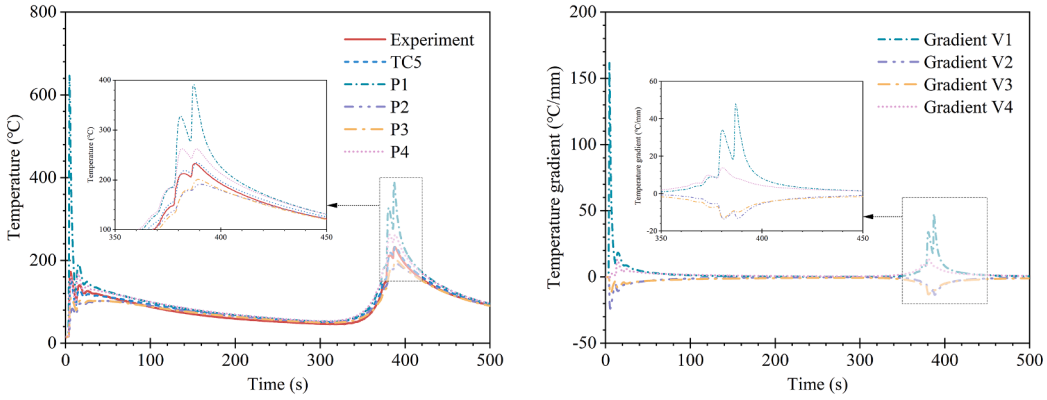

(a) Thermal cycles of TC5 (b) Thermal gradients of TC5

Fig. 26. Simulated thermal cycles and thermal gradients considering thermocouples alignment errors, up to 500 s.

thermal. For example, the peak temperature at Q1 reached 646.3 °C at 4.5 s, much higher than both simulated temperature (154.8 °C) and experimental value (173.2 °C) at TC5. Additionally, the temperature gradient along the V1 direction reached 161.6 °C/mm, far exceeding gradients in other directions. The gradient in the V1 direction dropped to 48.0 °C/mm at 386.8 s after the second deposition layer was complete.

Similarly, stress evolutions and stress gradients at SG1 are plotted in Fig. 27. For stress evolutions, as shown in Fig. 27(a), stress magnitudes were lower when nodes were closer to the welded wall (V1 direction). Stress gradients in opposite directions (V1 versus V2 and V3 versus V4) were nearly opposite. Unlike temperature gradients, stress gradients didn't decrease over time. The local maximum stress gradient in the V2 direction increased from 2.108 MPa/mm at 94.0 s to 5.443 MPa/mm at 210.4 s and 6.456 MPa/mm at 335.2 s, indicating that alignment-related errors in thermal stress measurements increased over time. This may explain why SG1 measurement continuously deviates from FE simulation result. This analysis highlights the importance of precise sensor placement to ensure accurate experimental data and its correlation with simulation outputs.

4.2.4. *Sequentially coupled thermal-stress analysis*

To quantify the sensitivity of the simulation results to computational techniques, another widely used model, the sequentially coupled (SC) model is performed, where transient temperatures evaluation precedes mechanical analysis to obtain the deformation and stress fields [44]. Usually, the FC model is much more time-consuming, and provides higher accuracy. The SC model was developed while keeping material and boundary parameters unchanged. For the SC model, for the heat transfer simulation, DC3D8 and DS4 elements were used for the solid and shell elements respectively. For the sequential static general simulation, C3D8R and S4R elements were adopted.

Fig. 28 and Fig. 29 present comparisons between the measurements from thermocouples TC1 and TC5, and strain gauges SG1 and SG2, and the numerical results for both FC and SC models. It can be observed that the thermal cycles of both models follow similar trend, but the temperatures obtained with the SC model are underestimated, because the effect of FE elements deformation on temperature is not considered. The SC model underestimates the first peak temperature of TC1 and TC5 by 36.8 % (230.1 °C versus 363.9 °C) and 38.7 % (94.9 °C versus 154.7 °C) respectively compared with the FC model. As a result of thermal underestimation, the simulated stress cycle amplitude is lower in the SC model. It's worth mentioning that the SC model displayed an 85.2 % reduction in computational time compared to the FC model. Therefore, although the thermal and stress fields in the SC model are underestimated, their accurate simulated trends provide a valuable indicator to reveal the thermal and stress evolutions considering the relatively low computational cost, especially for time-consuming simulations.

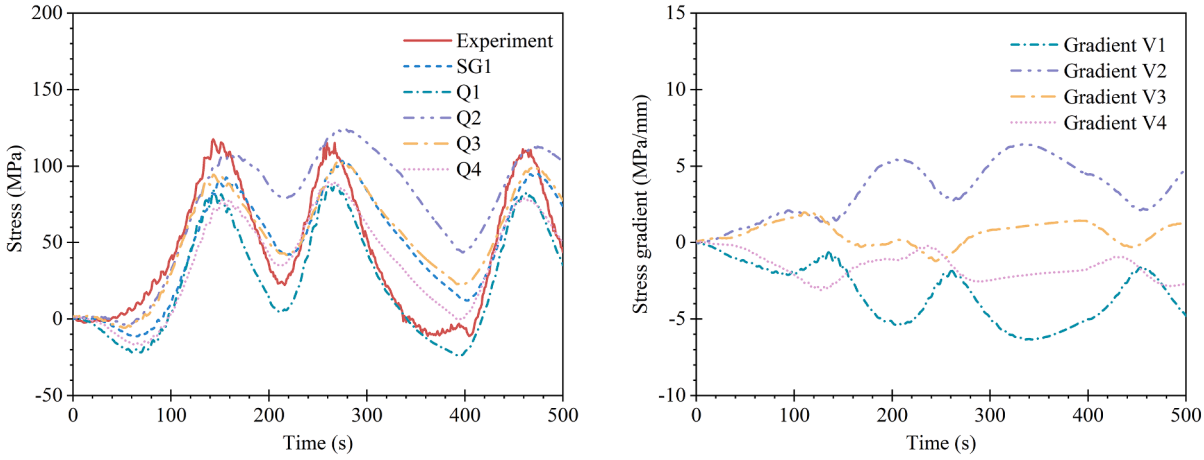

(a) Stress evolutions of SG1 (b) Stress gradients of SG1

Fig. 27. Simulated stress evolutions and stress gradients considering strain gauges alignment errors, up to 500 s.

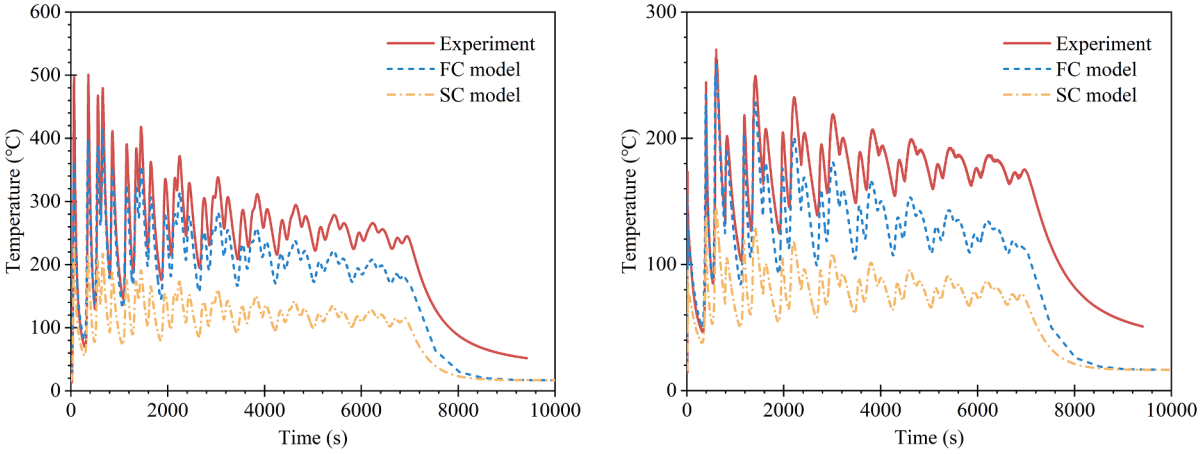

(a) Thermal cycles of TC1 (b) Thermal cycles of TC5

Fig. 28. Comparison of simulated thermal cycles based on FC and SC models.

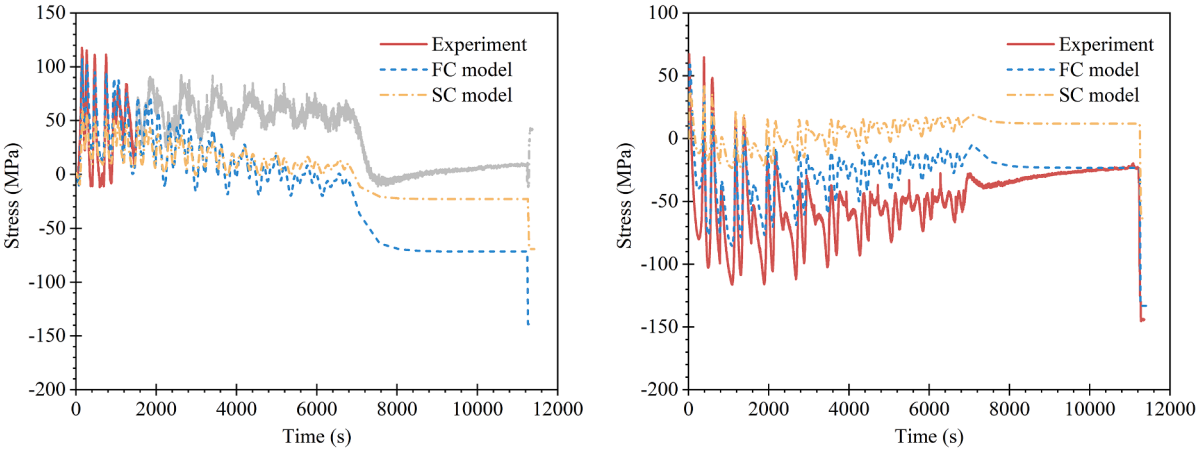

(a) Stress evolutions of SG1 (b) Stress evolutions of SG2

Fig. 29. Comparison of simulated stress evolutions based on FC and SC models.

5. Effect of boundary conditions on residual stress patterns

5.1. Stress development

To better illustrate the stress development within the component, Fig. 30 shows the longitudinal stress (S11) and transverse stress (S22) evolutions along lines AB, CD, and EF after depositing different layers. The locations of these lines are also depicted in Fig. 30, where line AB is the longitudinal centreline of the substrate's top surface (x – direction), line CD is parallel to the transverse centreline of the substrate's top surface (y – direction), and line EF is the vertical centreline through the substrate and welded specimen (z – direction). The letters in brackets on the horizontal axis indicate the endpoints of the lines, and the blue regions represent the areas of welded specimen. Along line AB, the longitudinal stresses exhibit a tension–compression-tension pattern, while the transverse stresses follow a compression-tension–compression pattern. The longitudinal and transverse stresses change drastically and reach their peak at the boundaries between the welded specimen and substrate, and the magnitude of stress increases with the number of layers. Along the free region of line CD, the longitudinal stresses transition from tensile to compressive with increasing deposition height, whereas the transverse stresses are always in a tensile state. The transition of stresses along CD crossing the model boundaries is also obvious. The stress values increase within the deposited specimen or decrease in the substrate region during deposition. The stress patterns are consistent with results in the literature [28,45]. Along line EF, the stress distributions of different deposition layers follow similar trends. Obvious stress transition can be identified between substrate and welded specimen boundary, where $z = 0$. For each curve, the magnitude of stress within the welded specimen ($z > 0$) increases with elevated height first, reaching their maximum, then drops, and the maximum stress occurs around the third or fourth layers before the final layer. Moreover, the stresses in the last layer decrease during deposition, and even shifts from tension to compression. Taking the transverse stress at SG2 as an example (see Fig. 30(f)), the stresses after the deposition of the 10th, 20th, 30th and 35th layers decrease from 126.8 MPa, 8.6 MPa, −46.0 MPa to −130.3 MPa. Similar phenomenon is also observed at SG1, see Fig. 30(e).

Due to springback, the stress field undergoes rapid redistribution after unclamping, which induces deformation of the specimen and residual stresses. A global overview and cross section of the simulated vertical deformation (U3) and residual stress distribution of the specimen under clamping (after full cooling) and after unclamping are shown in Fig. 31. The maximum vertical displacement is 0.597 mm in the central part of the substrate under clamping, and transfers to the end of the substrate after unclamping (1.590 mm). Meanwhile, a significant

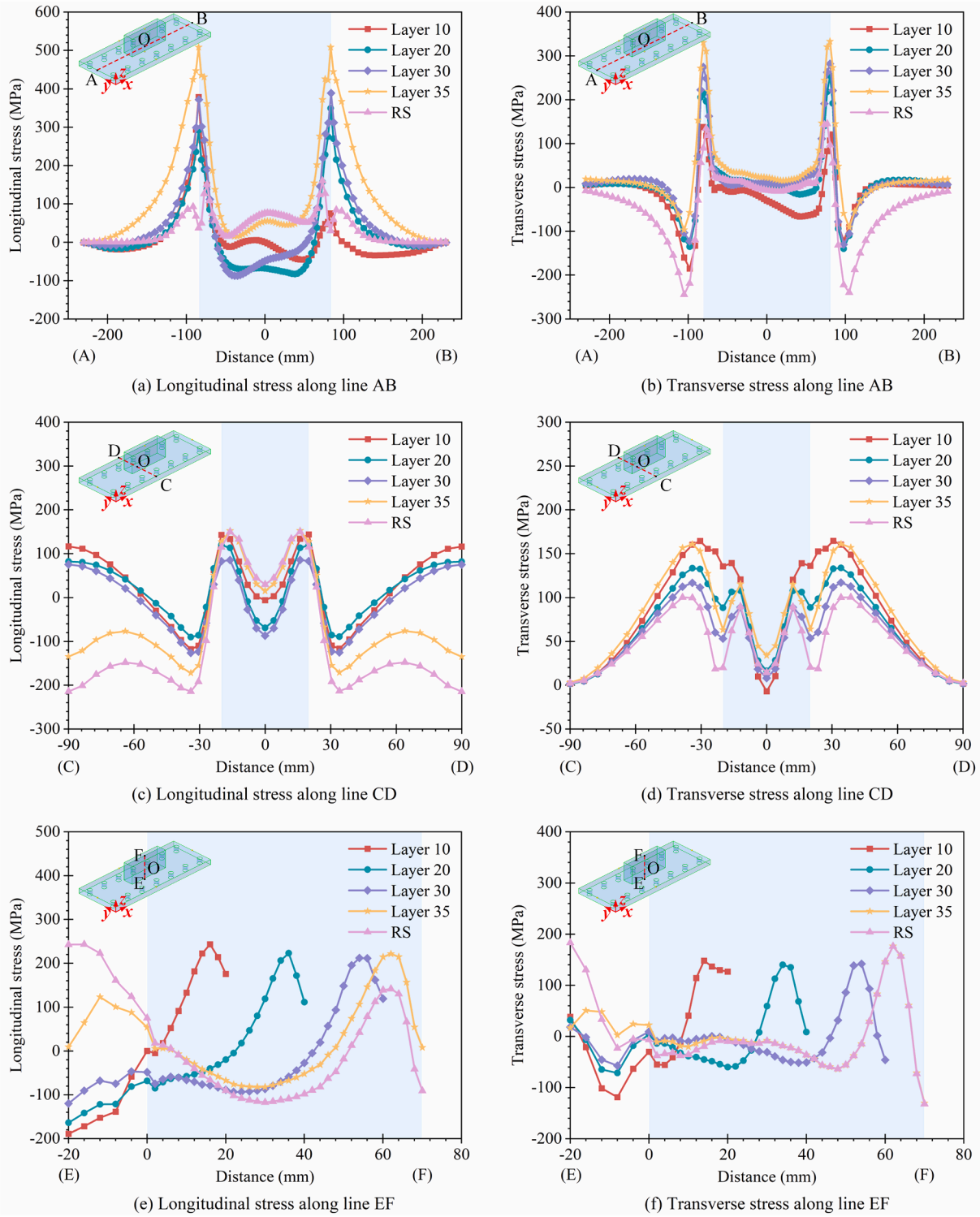

Fig. 30. Longitudinal and transverse stresses along the lines AB, CD and EF during deposition process.

drop of stresses around the connection region between the welded specimen and the substrate is observed. The stress distribution in the cross section, during the deposition stage, shows that the connection region on the substrate's top surface experienced tension stress, and that the opposite side, however, on the substrate's bottom surface underwent compression. After unclamping, the bottom is in tension, and the overall stress within the specimens is redistributed. The residual stress distributions along lines AB, CD and EF ("RS" curves) are displayed in Fig. 30. In most cases, the stress magnitude drops after unclamping (see "layer 35" curve versus "RS" curve in Fig. 30). The endpoints of line AB or CD do not bear transverse residual stress. Conversely, the longitudinal stress at points C and D transform from tension to compression with increasing deposition height. Additionally, the central point on the substrate's bottom surface (point E) was subjected to tension stress after unclamping, with S11 at 242.6 MPa and S22 at 183.2 MPa. Within the welded specimen, the transverse residual stress along line EF after

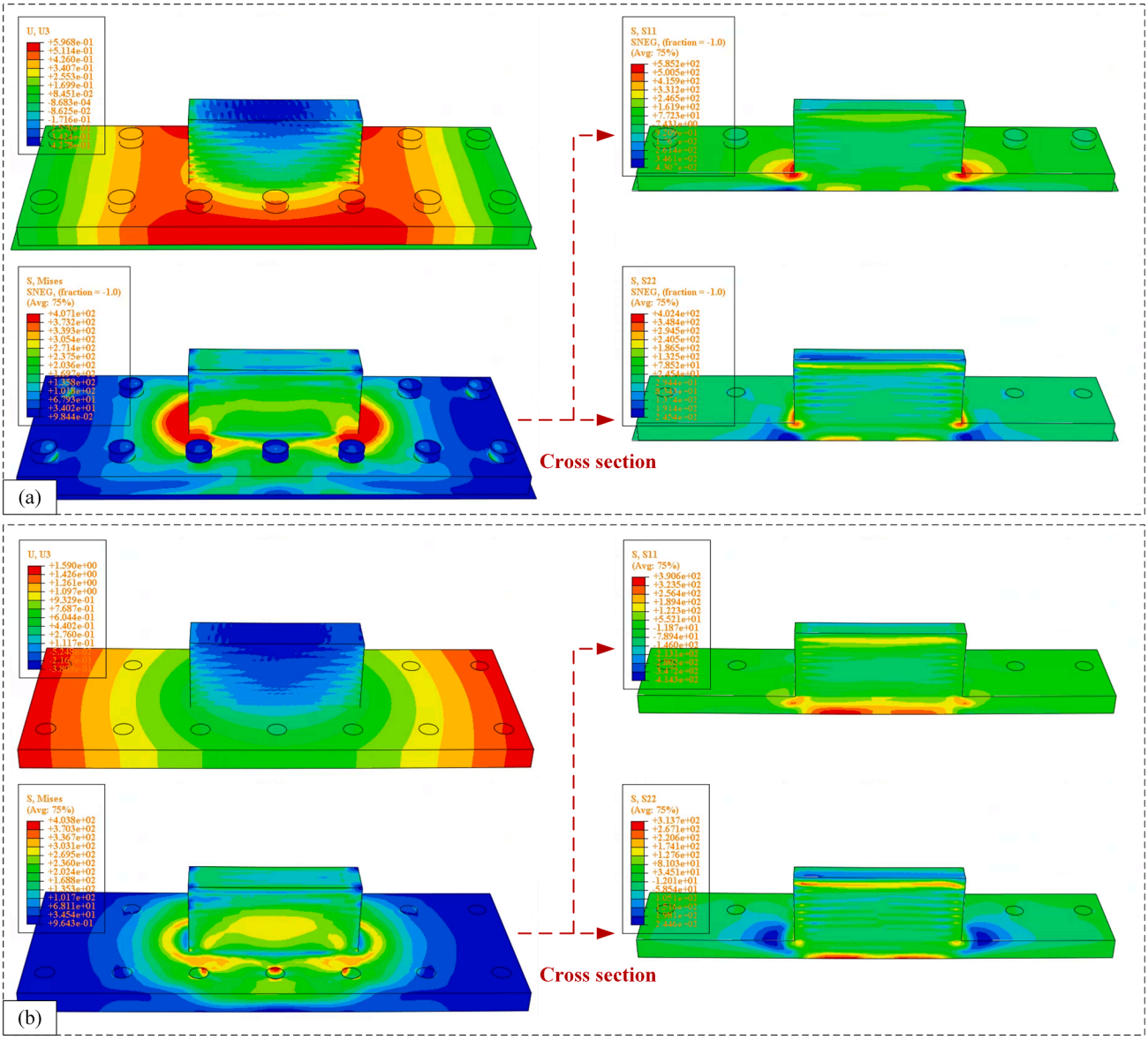

Fig. 31. Simulated deformation and residual stress under: (a) Clamping state; and (b) Unclamping state.

unclamping almost coincides with the stress distribution observed under clamping condition.

Boundary deformation between successive deposition layers was observed in both three-dimensional scanned profiles (measured using 3D laser scanning) and FE simulation results, as shown in Fig. 32. This deformation is an inherent characteristic of the WAAM process, driven primarily by cyclic thermal and mechanical effects. Each layer in WAAM undergoes significant thermal expansion during heating, followed by subsequent contraction during cooling. As new layers are deposited, they become constrained by the previously solidified layers, leading to localized thermal mismatch and strains at the layer boundaries. This cyclic process induces residual stresses at the interlayer interfaces, leading to plastic deformation and visible boundary distortions. Additionally, the rapid cooling rates at layer boundaries result in varied microstructures across layers, further contributing to uneven shrinkage and localized stress concentrations. These boundary deformations can affect the structural integrity, dimensional accuracy, and surface quality of the final component. To mitigate these effects, a combination of precise thermal management, interlayer cooling strategies, and post-process heat treatments is essential for relieving internal stresses. By employing advanced process controls and optimizing deposition strategies, it is possible to reduce boundary effects, thereby improving the overall quality and performance of WAAM-produced components.

The deformation of the specimen after unclamping is shown in Fig. 33 which compares the deformed profiles with the simulated deflections. Lines GH and IJ represent the longitudinal and transverse cross sections of the substrate's bottom surface, while polylines KLMN and OPQR correspond to the longitudinal and transverse cross sections of the deposited wall and the substrate's top surface. The creases in the experimental profile in Fig. 33(a) are the drilled reservations for the installation of the thermocouples TC1 ~ TC4, which were neglected in the FE model. It can be observed that excellent agreement between the computed deflections and the laser scanned profiles was achieved, validating the accuracy of the proposed FE model in simulating residual stress distribution. Additionally, after cutting the substrate from the workpiece using water jet cutting, the deposited wall was rescanned with the 3D laser scanner. This post-cutting scan captured the deformation caused by the release of residual stress in the component. The deformation redistribution in the deposited wall was compared with the simulated deformation along polylines LM and PQ, see Fig. 34. The close

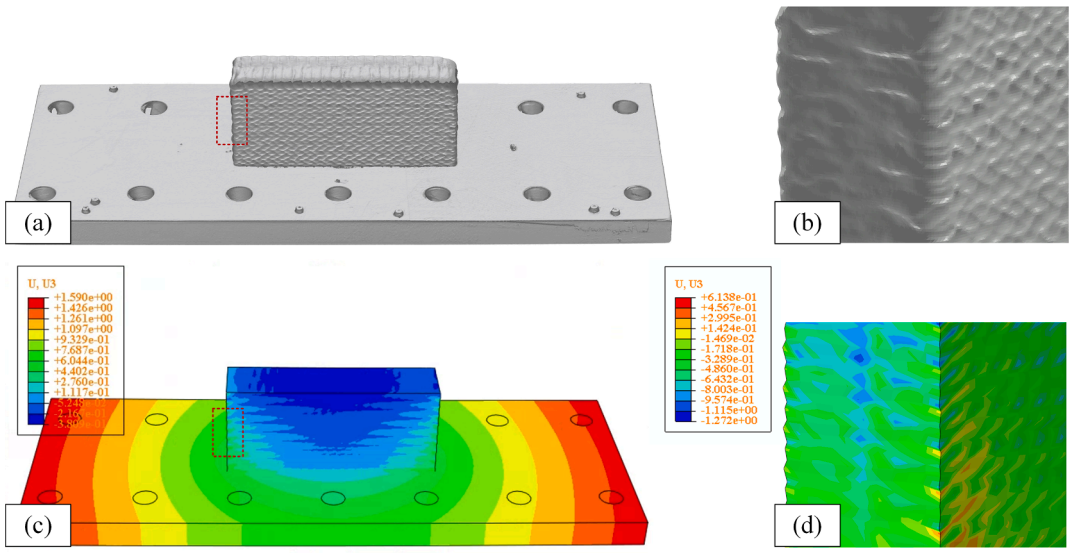

Fig. 32. Boundary deformation of successive deposition layers observed through: (a) and (b) Three-dimensional scanned profiles; and (c) and (d) FE simulated vertical deformation (U3).

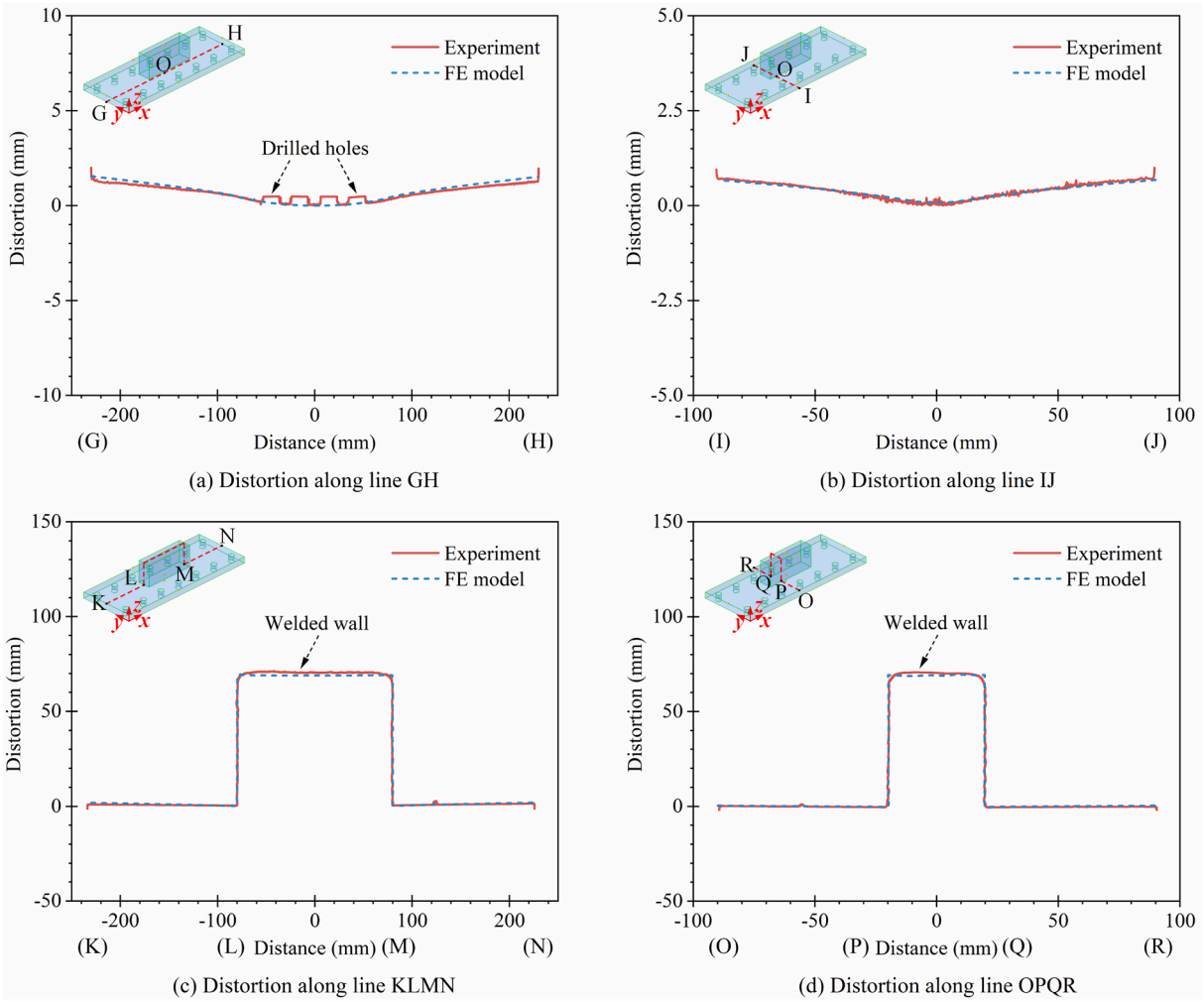

Fig. 33. Comparison of the three-dimensional scanned deformed profiles with the simulated deflections of the substrate and deposited wall after unclamping.

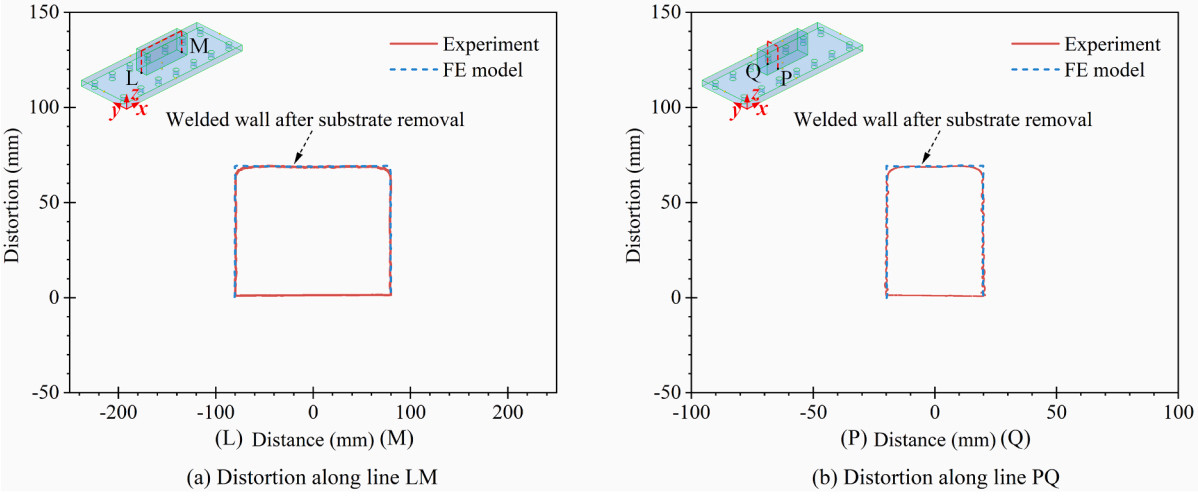

(a) Distortion along line LM (b) Distortion along line PQ

Fig. 34. Comparison of the three-dimensional scanned deformed profiles with the simulated deflections of the deposited wall after substrate removal.

match between the simulated and experimental profiles further validates the accuracy of the FE model in predicting residual stress distribution.

5.2. Bolt pretension force

Bolt joint is one of the most widely used joining methods between the platform and components during manufacturing process. The preload force presently applied on the bolts in the experiment was evaluated to be 10.2 kN (corresponding to a torque of 29.5 kNm) [46]. To investigate the effects of bolt preloads on stress development, deposition scenario without preload forces (namely "No-Preload") was simulated using both FC and SC models. The simulation results show that the pretension force has negligible impact on the thermal fields of CMT process, while ignoring bolt preloads would lead to large deviations in the stress fields. The stress evolutions obtained at SG1 and SG2 with and without bolt pretension forces are depicted in Fig. 35. The difference in simulated stresses at SG1 increases with time, while the difference at SG2 remains stable, revealing that longitudinal stress is more sensitive to bolt pretension force than transverse stress.

5.3. Substrate joint method

To investigate the effect of substrate joint method on the final residual stress distribution, two other commonly used substrate joint types were simulated [47,48]: (a) flexible boundary type with bolts to restrict the substrate movement; and (b) rigid boundary type using a thick substrate. The schematic of the two boundary conditions is shown in Fig. 36.

The thermal cycles and stress evolutions of models with different boundary conditions are shown in Fig. 37 and Fig. 38 respectively. The flexible boundary model provides temperature results highly similar to the FC model by setting same surface convection and radiation coefficients, while the rigid boundary model exhibits slightly lower temperature at deposition stage and higher temperature at cooling stage because the thick steel substrate can store large amounts of heat. For the stress cycles at SG1, the flexible boundary model has the lowest simulated transient stress as it is the least constrained model, and it shows similar trend to the FC model without preload. For the stress cycles at SG2, the flexible boundary model shows highly consistent results compared to the case of bolt joint without bolt pretension force. Among these models, the stress evolutions of the rigid boundary model show the least amplitude variation due to the highest stiffness. The differences of stress evolutions between different boundary conditions increase with time for the longitudinal stress, but remain stable for the transverse stress, indicating that the latter is less sensitive to boundary conditions.

The simulated deformation and residual stress distribution of both flexible and rigid boundary cases are displayed in Fig. 39. The rigid

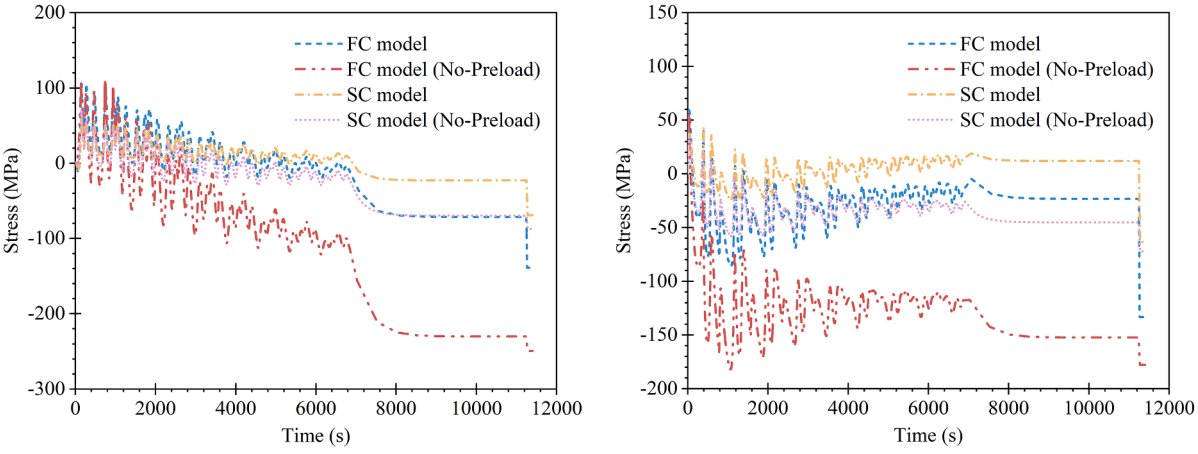

(a) Stress evolutions of SG1 (b) Stress evolutions of SG2

Fig. 35. Comparison of stress evolutions with different bolt pretension forces.

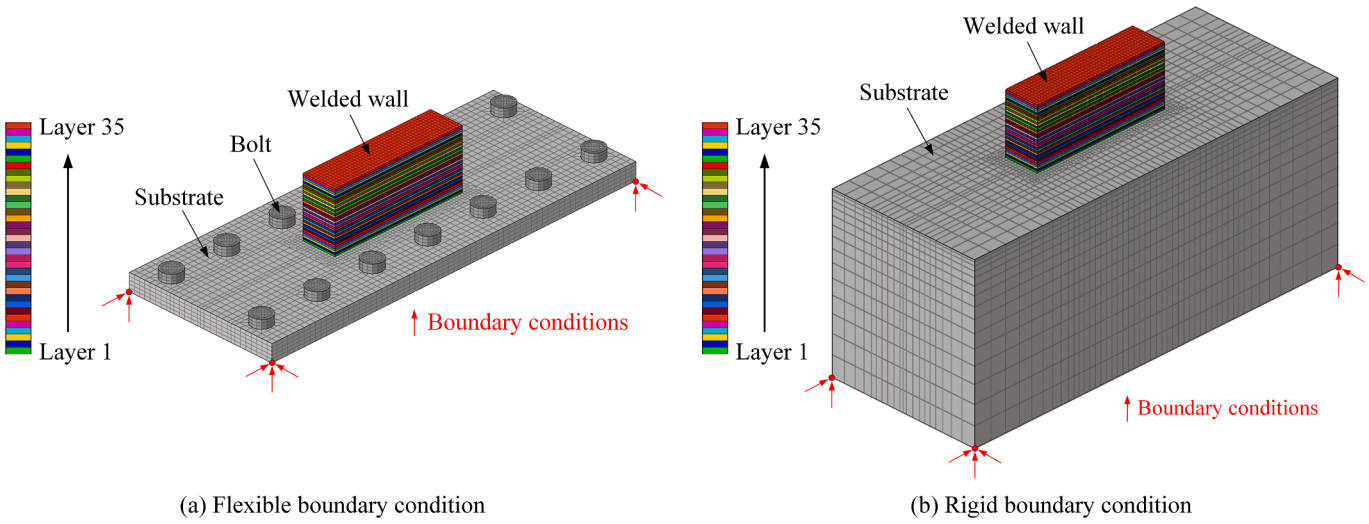

(a) Flexible boundary condition (b) Rigid boundary condition

Fig. 36. Illustration of different substrate joint methods.

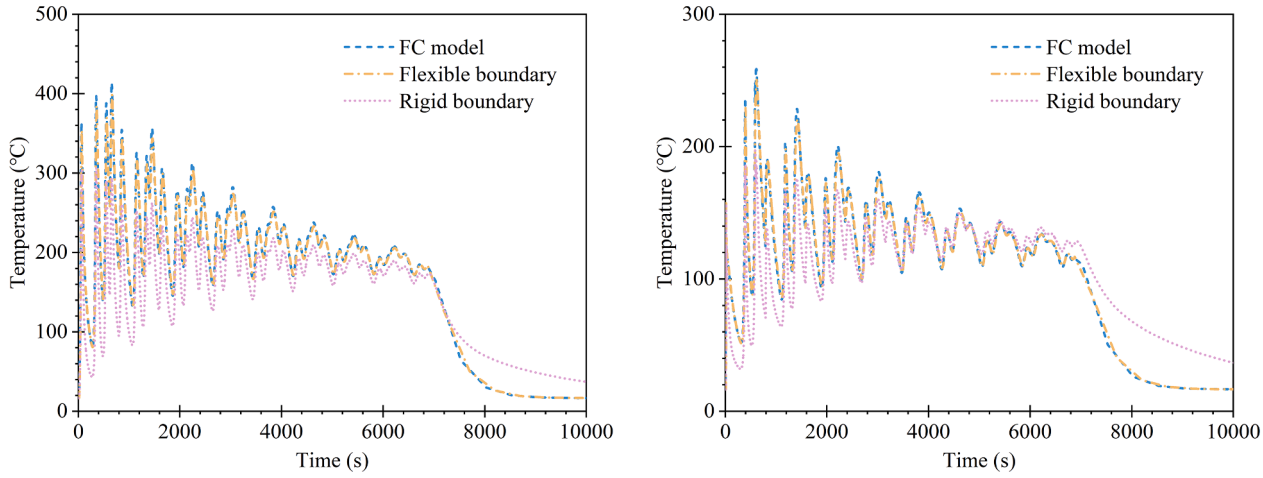

(a) Thermal cycles of TC1 (b) Thermal cycles of TC5

Fig. 37. Comparison of thermal cycles at TC1 and TC5 for FE models with different substrate joint methods.

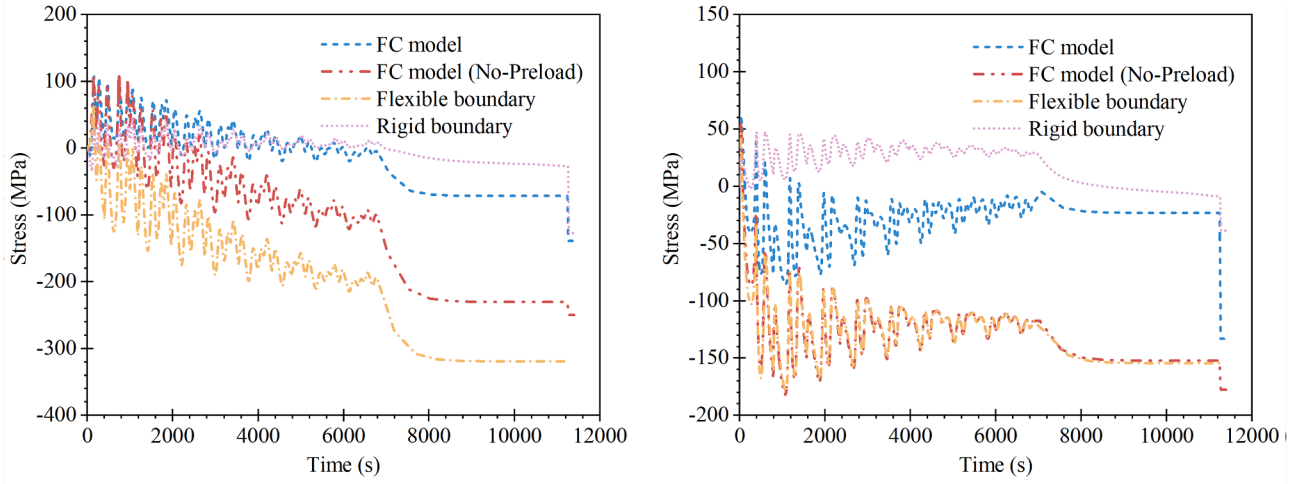

(a) Stress evolutions of SG1 (b) Stress evolutions of SG2

Fig. 38. Comparison of stress evolutions at SG1 and SG2 for FE models with different substrate joint methods.

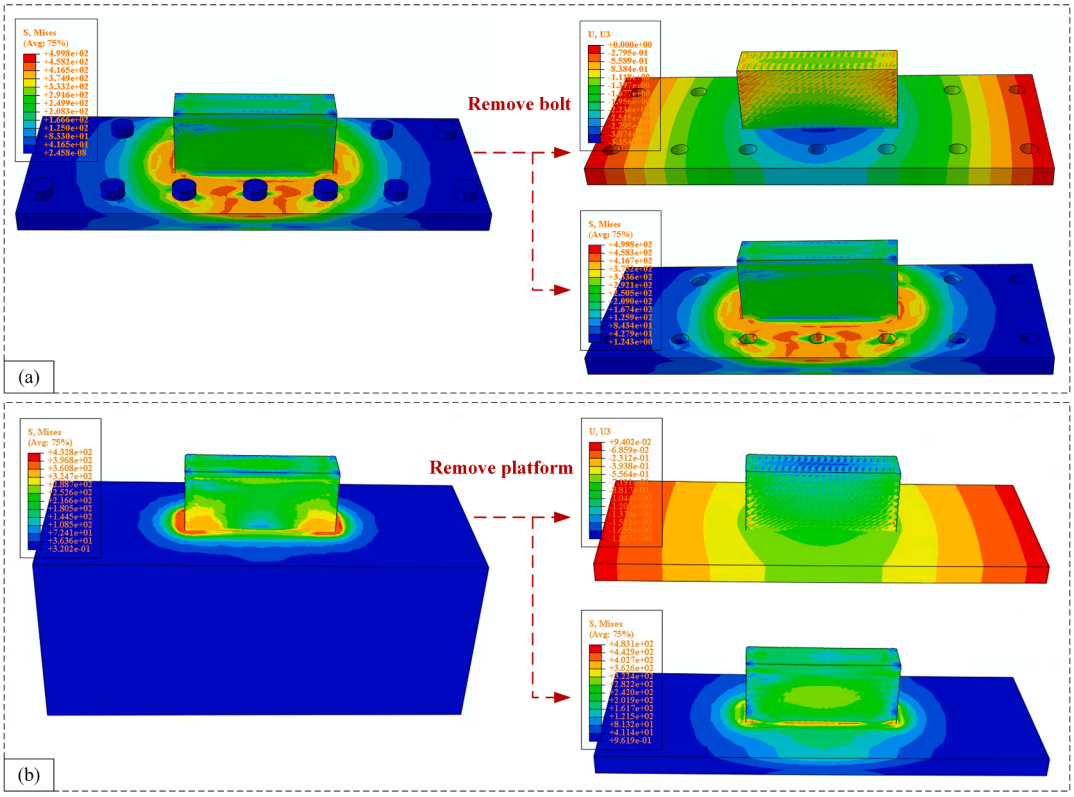

Fig. 39. Simulated deformation and residual stresses with: (a) Flexible boundary condition; and (b) Rigid boundary condition.

boundary condition leads to smaller deformation and higher residual stress than bolt joint (FC) model, which is expected when adopting a stiffer experimental system. Conversely, the flexible boundary deposition process displays larger deformation along the vertical direction due to fewer constraints. Meanwhile, the residual stress distribution of rigid boundary case is more concentrated in the connected region between the welded specimen and the substrate, with a higher residual stress gradient.

6. Discussion

Based on the analysis, it can be concluded that the thermal behaviour in the CMT process is not highly sensitive to boundary conditions, such as bolt pretension forces or substrate joint methods. However, thermal stress development is more sensitive to these boundary conditions, with longitudinal stresses showing greater sensitivity than transverse stresses. To further explore the effect of boundary conditions on residual stress distribution, Fig. 40 illustrates the residual stress along the centreline EF of specimens subjected to different boundary conditions. It can be observed that all the fully coupled models exhibit a similar residual stress pattern along the centreline, following a tension–compression-tension–compression trend from the bottom of the substrate (Point E) to the top surface of the deposited wall (Point F). A similar stress distribution pattern has also been reported by Yuan et al. [49], who found

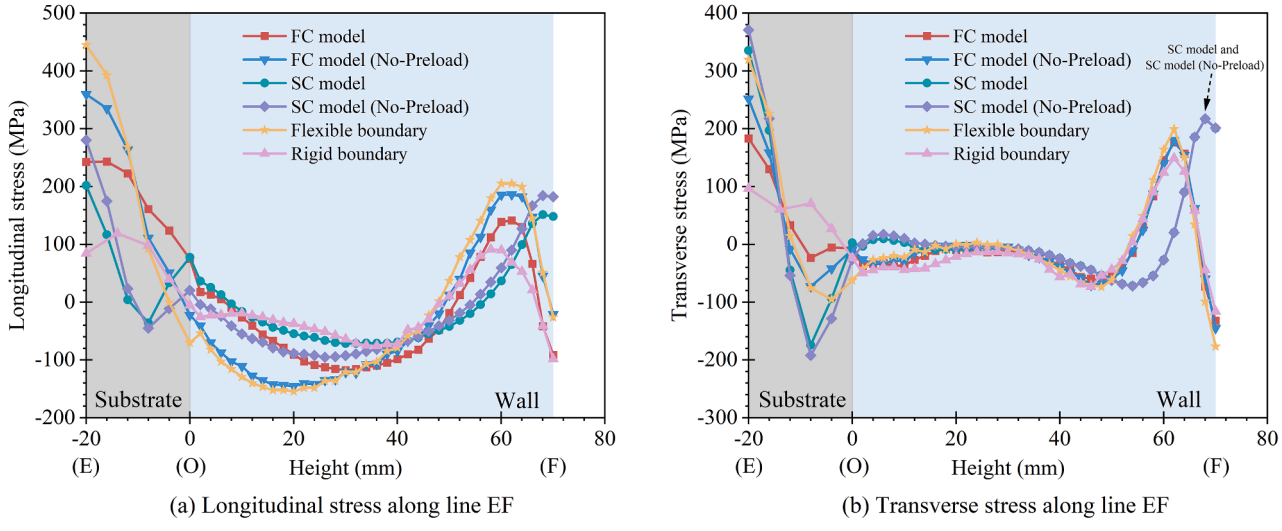

Fig. 40. Residual stress along line EF with different boundary conditions after unclamping.

that WAAM specimens, regardless of material, welding method or dimensions, can have the same stress distribution pattern along their height [49], aligning with the results shown in Fig. 40. The tensile stress in the substrate and the compressive stress at the top surface arise due to bending deflection after the clamps are released. Although the SC model achieves similar simulated trends to the FC model for the first 25 deposition layers, it deviates in layers 26 to 35 (corresponding to a height of 52 mm to 70 mm), indicating that the SC model can't accurately capture the residual stress distribution in the final few layers.

System stiffness has been reported as a key factor influencing the stress in WAAM specimens [49,50], which is consistent with our findings. Bolt pretension increases joint stiffness, helping to distribute stresses more evenly across the interface between the components. This clamping force prevents deformation and maintain component alignment during deposition, and also reduces the magnitude of residual stress at the substrate's bottom surface. By applying pretension, longitudinal tensile stress decreases from 359.7 MPa to 242.6 MPa in the FC model, and transverse tensile stress drops from 251.7 MPa to 183.2 MPa. Similarly, the residual stress at the bottom surface of the substrate is lowest under rigid boundary conditions, indicating higher system rigidity. The longitudinal residual stress at the substrate's bottom surface increases from 84.7 MPa (rigid boundary) to 242,6 MPa (FC model with preload) and up to 444.8 MPa (flexible boundary). The transverse residual stress follows a similar trend, rising from 96.7 MPa, 183.2 MPa to 319.5 MPa as boundary conditions become less constrained. Stress evolution patterns along different paths (lines AB, CD, and EF) during the deposition process are shown in Fig. 30. As the deposition height increases, the stiffness of the deposited wall also increases, causing stress patterns to change from almost full tension (10 layers) to compression-tension (20 layers and 30 layers) to compression-tension-slightly compression (35 layers) patterns at the clamping state. The influence of relative stiffness between the substrate and the deposited wall is consistent with findings in the literature [45,49–54]. Moreover, the further away from the substrate ($z = 0$), the impact of varying system stiffness on residual stress gradually diminishes, indicating that the substrate's stiffness becomes less influential. The transverse stress curves within the weldment are nearly overlapping under different boundary conditions, except for the SC model, where deviations are attributed to modelling inaccuracies.

The residual stress within the deposited wall after substrate removal was also analysed, see Fig. 41. After the substrate is removed, the residual stress along the centreline of the deposited wall follows a tension–compression-tension–compression pattern from the bottom to the top surface. At the bottom of the welded specimen ($z = 0$), small stress value is observed while the wall is still connected to the substrate, but both longitudinal and transverse stresses increase significantly after substrate removal. The evolution and distribution of residual stress within deposited wall after substrate removal are highly consistent with literature [54]. The stress distributions within the weldment are similar across all boundary conditions, suggesting that the impact of the substrate joint methods is partly relieved by substrate removal. Still, the FC model with preload shows slightly lower residual stress, with longitudinal and transverse tensile stresses of 162.1 MPa and 273.7 MPa at $z = 0$, compared to 229.8 MPa and 329.5 MPa in the FC model without preload. The rigid boundary model exhibits the lowest residual stresses, with longitudinal and transverse tensions of 48.1 MPa and 220.7 MPa, respectively. In the last layer, the longitudinal stresses for all fully coupled models range between −138.8 MPa and −107.5 MPa, while transverse stresses are within the range of −175.5 MPa and −115.1 MPa. Similar to the behaviour before substrate removal, the SC models fail to accurately capture the stress distribution in the final few layers. Additionally, the residual stresses in the layers of 26 to 35 (deposition height of 52 mm to 70 mm) show little variation after substrate removal, further confirming that the influence of substrate stiffness stabilizes once the deposition height reaches a certain level.

The maximum residual stresses within the deposited specimen after substrate removal under different boundary conditions are summarised in Table 7. The maximum von Mises stresses within the weldment across all boundary conditions are approximately 300 MPa, with a maximum relative difference of 11.6 %. Specifically, the FC model with preload shows a maximum stress of 285.6 MPa, while the flexible boundary condition results in a maximum stress of 318.8 MPa. Despite the variations, the residual stress distributions after substrate removal exhibit similar patterns across all boundary conditions. Typically, the residual stress distributions of the FC model are illustrated in Fig. 42. In all cases, the maximum S11 (longitudinal) and S22 (transverse) stresses are located at the bottom surface of the welded specimen, i.e., the region originally connected to the substrate at $z = 0$. Meanwhile, the maximum S33 and von Mises stresses appear on the longitudinal side surface of the weldment. This finding highlights the importance of carefully considering boundary conditions during the deposition process. If the substrate intended to remain as part of the final structure with the deposited wall, boundary conditions such as thickness of substrate, bolt pretension force and joint methods should be carefully selected to ensure an optimal residual stress distribution. In contrast, if the focus is solely on the residual stress distribution within the deposited component and the substrate will be removed after the deposition is complete, more flexible boundary conditions can be used. This is because the influence of

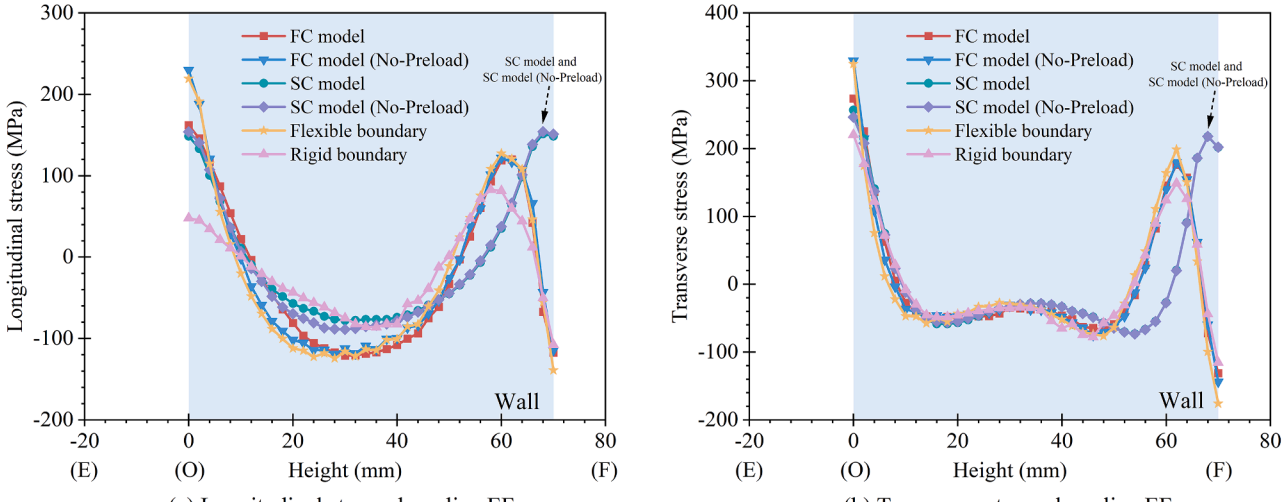

(a) Longitudinal stress along line EF

(b) Transverse stress along line EF

Fig. 41. Residual stress along line EF under different boundary conditions after substrate removal.

Table 7
Maximum residual stresses within the weldment calculated by different models after substrate removal.

Model	FC	SC	FC (No-Preload)	SC (No-Preload)	Flexible boundary	Rigid boundary
S11 [MPa]	212.8	183.8	253.5	182.1	263.1	259.4
S22 [MPa]	302.3	279.9	340.8	280.0	346.3	291.7
S33 [MPa]	289.0	327.7	291.0	322.0	289.5	318.8
Von Mises [MPa]	285.6	308.8	308.7	299.1	303.8	318.8

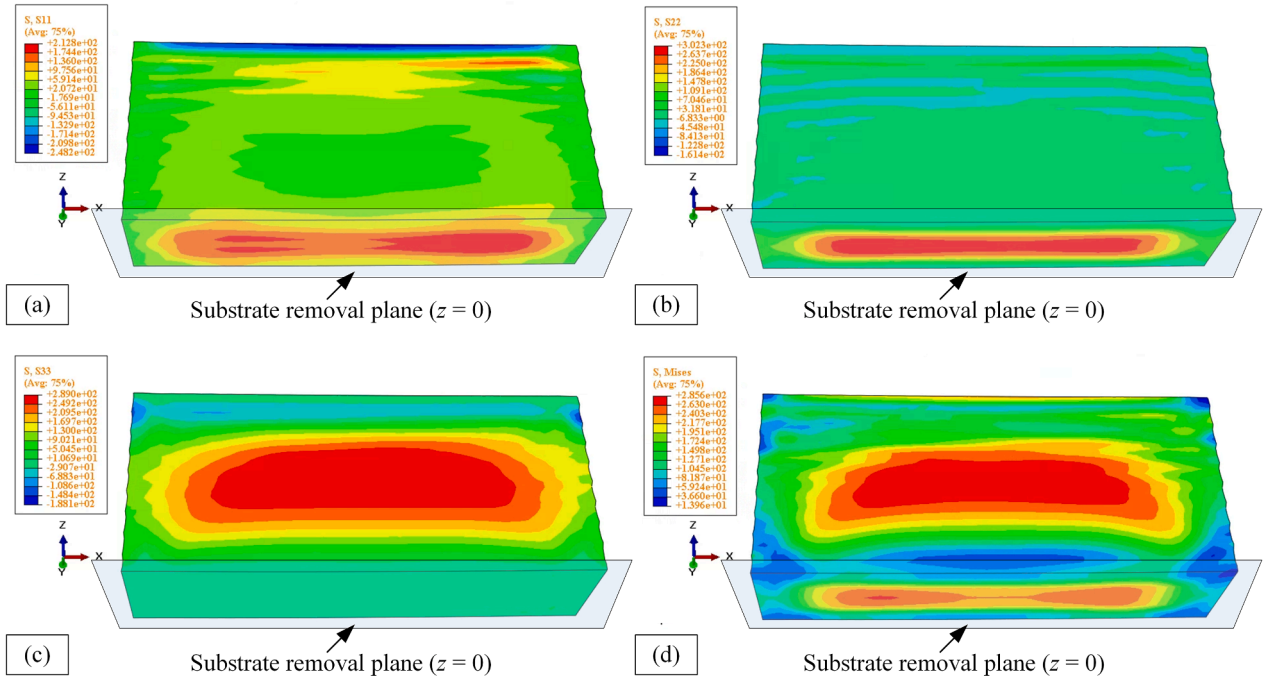

Fig. 42. Residual stress redistribution of FC model after substrate removal: (a) S11; (b) S22; (c) S33; and (d) Von Mises stress.

boundary conditions on the residual stress distribution in the weldment can be partially mitigated by removing the substrate.

7. Conclusions

This paper investigates thermal and stress developments during cold metal transfer (CMT)-based wire arc additive manufacturing (WAAM) of steel components, through a comprehensive finite element (FE) modelling approach. CMT deposition of multi-layer flat specimens served as a foundation for this research. A detailed experimental exploration of temperature development, strain variation and deformation across the component was conducted employing a combination of FLIR thermography, strain gauges, and a three-dimensional laser scanner, the results of which were used to validate the numerical model. The developed FE model is described in detail, and enables to characterise the thermal and stress fields development in CMT-based WAAM unalloyed S355 specimens. The sensitivity of residual stress patterns to boundary conditions, including bolt pretension forces and substrate joint methods, is then investigated. Based on the results of this study, the following conclusions can be drawn:

1) The proposed three-dimensional FE model can simulate the temperature and stress development of CMT-based WAAM with great accuracy. Springback after bolt removal can be precisely simulated.

2) The sensitivity of the FE model to ambient temperature, element activation strategies, alignment errors of thermocouples and strain gauges, and sequentially coupled approach is analysed.

3) Mechanical boundary conditions, such as bolt pretension force and substrate joint methods, have negligible impact on the thermal field development. However, both longitudinal and transverse residual stresses vary depending on the nature of the constraints on substrate.

4) The residual stress distributions within the weldment after unclamping and after substrate removal under different boundary conditions are discussed in detail, providing an insight into controlling the residual stress within the weldment.

5) The residual stress patterns redistribute in a similar manner after substrate removal, and the maximum relative difference between them is 11.6 %, which means that removing the substrate partly alleviate the prior influence of a rigid or more flexible substrate.

This research lays a solid foundation for understanding the mechanical performance of more complex structures and provides an effective tool to optimize the heat accumulation and residual stress in WAAM components without performing expensive trial and error operations. In future studies, the process parameters optimization will be performed based on the proposed FE model, which serves as a valuable source of data.

CRediT authorship contribution statement

Xiongfeng Ruan: Writing – review & editing, Writing – original draft, Visualization, Validation, Software, Resources, Methodology, Investigation, Formal analysis, Data curation, Conceptualization. **Burak Karabulut:** Writing – review & editing, Writing – original draft, Software, Investigation, Formal analysis, Conceptualization. **Scott MacDonald:** Writing – review & editing, Resources, Investigation. **Jelena Dobrić:** Writing – review & editing, Supervision, Resources. **Barbara Rossi:** Writing – review & editing, Supervision, Resources, Project administration, Methodology, Funding acquisition, Conceptualization.

Declaration of competing interest

The authors declare that they have no known competing financial interests or personal relationships that could have appeared to influence the work reported in this paper.

Acknowledgements

We would like to gratefully acknowledge Research Foundation Flanders (FWO) for funding of the post-doctoral fellowship "1256522 N". We would also like to thank Whittaker Engineering for their important input during the experimental investigations. We wish especially to thank Ken Whittaker for their unrelenting dedication to the accomplishment of our experiments.

Data availability

Data will be made available on request.

References

[1] B. Donaldson, The Hidden Complexities of Wire Arc Additive Manufacturing, (2020). https://www.additivemanufacturing.media/articles/the-hidden-complexities-of-wire-arc-additive-manufacturing/template.
[2] Meuselwitz-guss, Rotor hub, (n.d.). https://www.meuselwitz-guss.de/en/products/production-areas/heavy-casting/heavy-casting/news/rotor-hub-1/?tx_news_pi1%5Bcontroller%5D=News&tx_news_pi1%5Baction%5D=detail&cHash=de914e943a2a287703db67dc786de3b2.
[3] Gainza forge, Self reinforced stainless steel flanges, (n.d.). http://gainzaforge.com/products/flanges-self-reinforced-flanges/.
[4] Damen, World's first class approved 3D printed Ship's propeller unveiled, (n.d.). https://www.damen.com/en/news/2017/11/worlds_first_class_approved_3d_printed_ships_propeller_unveiled.
[5] U. Bhakthavatchalam, K. Ganeshmurthy, A. Jaisooriyan, Additive Manufacturing Using MIG Welding, International Journal of Research in Engineering, Science and Management 1 (2018).
[6] C. Buchanan, L. Gardner, Metal 3D printing in construction: A review of methods, research, applications, opportunities and challenges, Eng Struct 180 (2019) 332–348, https://doi.org/10.1016/j.engstruct.2018.11.045.
[7] S. Galjaard, S. Hofman, S. Ren, New Opportunities to Optimize Structural Designs in Metal by Using Additive Manufacturing, in: P. Block, J. Knippers, N.J. Mitra, W. Wang (Eds.), Advances in Architectural Geometry 2014, Springer International Publishing, Cham, 2015, pp. 79–93.
[8] S.W. Williams, F. Martina, A.C. Addison, J. Ding, G. Pardal, P. Colegrove, Wire + Arc additive manufacturing, Materials Science and Technology (united Kingdom) 32 (2016) 641–647, https://doi.org/10.1179/1743284715Y.0000000073.
[9] H. Mu, F. He, L. Yuan, P. Commins, H. Wang, Z. Pan, Toward a smart wire arc additive manufacturing system: A review on current developments and a framework of digital twin, J Manuf Syst 67 (2023) 174–189, https://doi.org/10.1016/J.JMSY.2023.01.012.
[10] C.R. Cunningham, J.M. Flynn, A. Shokrani, V. Dhokia, S.T. Newman, Invited review article: Strategies and processes for high quality wire arc additive manufacturing, Addit Manuf 22 (2018) 672–686, https://doi.org/10.1016/j.addma.2018.06.020.
[11] F. Montevecchi, G. Venturini, A. Scippa, G. Campatelli, Finite Element Modelling of Wire-arc-additive-manufacturing Process, Procedia CIRP 55 (2016) 109–114, https://doi.org/10.1016/j.procir.2016.08.024.
[12] J.L.Z. Li, M.R. Alkahari, N.A.B. Rosli, R. Hasan, M.N. Sudin, F.R. Ramli, Review of wire arc additive manufacturing for 3d metal printing, Int. J. Autom. Technol. 13 (2019) 346–353, https://doi.org/10.20965/ijat.2019.p0346.
[13] S. Selvi, A. Vishvaksenan, E. Rajasekar, Cold metal transfer (CMT) technology - An overview, Def. Technol. 14 (2018) 28–44, https://doi.org/10.1016/j.dt.2017.08.002.
[14] S. Cadiou, M. Courtois, M. Carin, W.B.-A. Manufacturing, undefined 2020, 3D heat transfer, fluid flow and electromagnetic model for cold metal transfer wire arc additive manufacturing (Cmt-Waam), Elsevier (n.d.). https://www.sciencedirect.com/science/article/pii/S2214860420309131 (accessed September 28, 2023).
[15] W. Hackenhaar, J.A.E. Mazzaferro, F. Montevecchi, G. Campatelli, An experimental-numerical study of active cooling in wire arc additive manufacturing, J Manuf Process 52 (2020) 58–65, https://doi.org/10.1016/j.jmapro.2020.01.051.
[16] R. Pramod, S. Mohan Kumar, B. Girinath, A. Rajesh Kannanc, N. Pravin Kumar, N. Siva Shanmugam, Fabrication, characterisation, and finite element analysis of cold metal transfer-based wire and arc additive-manufactured aluminium alloy, Weld. World 73 (2021) 331–350.
[17] M. Bayat, W. Dong, J. Thorborg, A.C. To, J.H. Hattel, A review of multi-scale and multi-physics simulations of metal additive manufacturing processes with focus on modeling strategies, Addit Manuf 47 (2021) 102278, https://doi.org/10.1016/j.addma.2021.102278.
[18] J. Ding, P. Colegrove, J. Mehnen, S. Ganguly, P.M.S. Almeida, F. Wang, S. Williams, Thermo-mechanical analysis of Wire and Arc Additive Layer Manufacturing process on large multi-layer parts, Comput Mater Sci 50 (2011) 3315–3322, https://doi.org/10.1016/j.commatsci.2011.06.023.
[19] S. Cadiou, M. Courtois, M. Carin, … W.B.-I.J. of, undefined 2020, Heat transfer, fluid flow and electromagnetic model of droplets generation and melt pool behaviour for wire arc additive manufacturing, Elsevier (n.d.). https://www.sciencedirect.com/science/article/pii/S0017931019345958 (accessed November 5, 2023).
[20] R. Geng, J. Du, Z. Wei, N. Ma, Multiscale modelling of microstructure, micro-segregation, and local mechanical properties of Al-Cu alloys in wire and arc additive manufacturing, Addit Manuf 36 (2020) 101735, https://doi.org/10.1016/j.addma.2020.101735.
[21] F. Hejripour, F. Binesh, M. Hebel, D.K. Aidun, Thermal modeling and characterization of wire arc additive manufactured duplex stainless steel, J Mater Process Technol 272 (2019) 58–71, https://doi.org/10.1016/j.jmatprotec.2019.05.003.
[22] L. Wang, Y. Wei, J. Chen, W. Zhao, Macro-micro modeling and simulation on columnar grains growth in the laser welding pool of aluminum alloy, Int J Heat Mass Transf 123 (2018) 826–838, https://doi.org/10.1016/j.ijheatmasstransfer.2018.03.037.
[23] S. Srivastava, R.K. Garg, V.S. Sharma, A. Sachdeva, Measurement and Mitigation of Residual Stress in Wire-Arc Additive Manufacturing: A Review of Macro-Scale Continuum Modelling Approach, Arch. Comput. Meth. Eng. 28 (2021) 3491–3515, https://doi.org/10.1007/s11831-020-09511-4.
[24] F. Incropera, D. DeWitt, T. Bergman, A. Lavine, Fundamentals of heat and mass transfer, (1996). http://www.mid-contracting.com/sites/default/files/webform/careers_webform/_sid_/pdf-fundamentals-of-heat-and-mass-transfer-frank-p-incropera-david-p-dewitt-pdf-download-free-book-7841c05.pdf (accessed October 6, 2024).
[25] D. Deng, H. Murakawa, Numerical simulation of temperature field and residual stress in multi-pass welds in stainless steel pipe and comparison with experimental measurements, Comput Mater Sci 37 (2006) 269–277, https://doi.org/10.1016/j.commatsci.2005.07.007.
[26] A. Ravisankar, S.K. Velaga, G. Rajput, S. Venugopal, Influence of welding speed and power on residual stress during gas tungsten arc welding (GTAW) of thin sections with constant heat input: A study using numerical simulation and experimental validation, J Manuf Process 16 (2014) 200–211, https://doi.org/10.1016/j.jmapro.2013.11.002.
[27] J. Xiong, Y. Lei, R. Li, Finite element analysis and experimental validation of thermal behavior for thin-walled parts in GMAW-based additive manufacturing with various substrate preheating temperatures, Appl Therm Eng 126 (2017) 43–52, https://doi.org/10.1016/j.applthermaleng.2017.07.168.
[28] R. Li, G. Wang, X. Zhao, F. Dai, C. Huang, M. Zhang, X. Chen, H. Song, H. Zhang, Effect of path strategy on residual stress and distortion in laser and cold metal transfer hybrid additive manufacturing, Addit Manuf 46 (2021) 102203, https://doi.org/10.1016/j.addma.2021.102203.
[29] H. Huang, N. Ma, J. Chen, Z. Feng, H. Murakawa, Toward large-scale simulation of residual stress and distortion in wire and arc additive manufacturing, Addit Manuf 34 (2020) 101248, https://doi.org/10.1016/j.addma.2020.101248.
[30] W. Dong, X. Liang, Q. Chen, S. Hinnebusch, Z. Zhou, A.C. To, A new procedure for implementing the modified inherent strain method with improved accuracy in predicting both residual stress and deformation for laser powder bed fusion, Addit Manuf 47 (2021) 102345, https://doi.org/10.1016/j.addma.2021.102345.
[31] X. Liang, L. Cheng, Q. Chen, Q. Yang, A.C. To, A modified method for estimating inherent strains from detailed process simulation for fast residual distortion prediction of single-walled structures fabricated by directed energy deposition, Addit Manuf 23 (2018) 471–486, https://doi.org/10.1016/j.addma.2018.08.029.
[32] C. Cambon, S. Rouquette, I. Bendaoud, C. Bordreuil, R. Wimpory, F. Soulie, Thermo-mechanical simulation of overlaid layers made with wire + arc additive manufacturing and GMAW-cold metal transfer, Weld. World 64 (2020) 1427–1435, https://doi.org/10.1007/s40194-020-00951-x.
[33] Z. Luo, Y. Zhao, A survey of finite element analysis of temperature and thermal stress fields in powder bed fusion Additive Manufacturing, Addit Manuf 21 (2018) 318–332, https://doi.org/10.1016/j.addma.2018.03.022.
[34] J. Ding, P. Colegrove, J. Mehnen, S. Williams, F. Wang, P.S. Almeida, A computationally efficient finite element model of wire and arc additive manufacture, Int. J. Adv. Manuf. Technol. 70 (2014) 227–236, https://doi.org/10.1007/s00170-013-5261-x.
[35] R. Kawalkar, H.K. Dubey, S.P. Lokhande, Wire arc additive manufacturing: A brief review on advancements in addressing industrial challenges incurred with processing metallic alloys, Mater Today Proc 50 (2022) 1971–1978, https://doi.org/10.1016/J.MATPR.2021.09.329.
[36] W. Jin, C. Zhang, S. Jin, Y. Tian, D. Wellmann, W. Liu, Wire Arc Additive Manufacturing of Stainless Steels: A Review, Applied Sciences 2020, Vol. 10, Page 1563 10 (2020) 1563. doi: 10.3390/APP10051563.
[37] T.A. Rodrigues, V. Duarte, R.M. Miranda, T.G. Santos, J.P. Oliveira, Current Status and Perspectives on Wire and Arc Additive Manufacturing (WAAM), Materials 12 (2019), https://doi.org/10.3390/MA12071121.
[38] F. Montevecchi, G. Venturini, N. Grossi, A. Scippa, G. Campatelli, Idle time selection for wire-arc additive manufacturing: A finite element-based technique, Addit Manuf 21 (2018) 479–486, https://doi.org/10.1016/j.addma.2018.01.007.
[39] D. Deng, H. Murakawa, W. Liang, Numerical simulation of welding distortion in large structures, Comput Methods Appl Mech Eng 196 (2007) 4613–4627, https://doi.org/10.1016/j.cma.2007.05.023.
[40] M. Chiumenti, M. Cervera, A. Salmi, C. Agelet de Saracibar, N. Dialami, K. Matsui, Finite element modeling of multi-pass welding and shaped metal deposition

processes, Comput Methods Appl Mech Eng 199 (2010) 2343–2359, https://doi.org/10.1016/j.cma.2010.02.018.
[41] F.W.C. Farias, J. da Cruz Payão Filho, V.H.P. Moraes e Oliveira, Prediction of the interpass temperature of a wire arc additive manufactured wall: FEM simulations and artificial neural network, Addit Manuf 48 (2021). doi: 10.1016/j.addma.2021.102387.
[42] R. Escribano-García, N. Rodriguez, O. Zubiri, J. Piccini, I. Setien, 3D numerical simulation of GMAW Cold Metal Transfer using response surface methodology, J Manuf Process 76 (2022) 656–665, https://doi.org/10.1016/j.jmapro.2022.02.043.
[43] S.K. Bate, R. Charles, A. Warren, Finite element analysis of a single bead-on-plate specimen using SYSWELD, Int. J. Press. Vessel. Pip. 86 (2009) 73–78, https://doi.org/10.1016/j.ijpvp.2008.11.006.
[44] H. Bikas, P. Stavropoulos, G. Chryssolouris, Additive manufacturing methods and modeling approaches: A critical review, Int. J. Adv. Manuf. Technol. 83 (2016) 389–405, https://doi.org/10.1007/s00170-015-7576-2.
[45] J. Sun, J. Hensel, M. Köhler, K.D.-J. of M. Processes, undefined 2021, Residual stress in wire and arc additively manufactured aluminum components, ElsevierJ Sun, J Hensel, M Köhler, K DilgerJournal of Manufacturing Processes, 2021•Elsevier (n.d.). https://www.sciencedirect.com/science/article/pii/S1526612521001079 (accessed October 22, 2024).
[46] K. Brown, C. Morrow, S. Durbin, A. Baca, Guideline for bolted joint design and analysis: version 1.0., (2008). https://www.osti.gov/biblio/929124 (accessed November 6, 2023).
[47] J. Sun, J. Hensel, M. Köhler, K. Dilger, Residual stress in wire and arc additively manufactured aluminum components, J Manuf Process 65 (2021) 97–111, https://doi.org/10.1016/j.jmapro.2021.02.021.
[48] G. Fu, M.I. Lourenco, M. Duan, S.F. Estefen, Effect of boundary conditions on residual stress and distortion in T-joint welds, J Constr Steel Res 102 (2014) 121–135, https://doi.org/10.1016/j.jcsr.2014.07.008.
[49] Q. Yuan, C. Liu, W. Wang, M. Wang, Residual stress distribution in a large specimen fabricated by wire-arc additive manufacturing, Sci. Technol. Weld. Join. 28 (2023) 137–144, https://doi.org/10.1080/13621718.2022.2134963.
[50] J. Zhang, X. Wang, S. Paddea, X.Z.-M.& Design, undefined 2016, Fatigue crack propagation behaviour in wire+ arc additive manufactured Ti-6Al-4V: Effects of microstructure and residual stress, ElsevierJ Zhang, X Wang, S Paddea, X ZhangMaterials & Design, 2016•Elsevier (n.d.). https://www.sciencedirect.com/science/article/pii/S026412751530719X (accessed October 22, 2024).
[51] J. Hönnige, P. Colegrove, B. Ahmad, M.F.-M.& Design, undefined 2018, Residual stress and texture control in Ti-6Al-4V wire+ arc additively manufactured intersections by stress relief and rolling, ElsevierJR Hönnige, PA Colegrove, B Ahmad, ME Fitzpatrick, S Ganguly, TL Lee, SW WilliamsMaterials & Design, 2018•Elsevier (n.d.). https://www.sciencedirect.com/science/article/pii/S0264127518302557 (accessed October 22, 2024).
[52] S. Srivastava, · Rajiv, K. Garg, V.S. Sharma, · Anish Sachdeva, Measurement and mitigation of residual stress in wire-arc additive manufacturing: A review of macro-scale continuum modelling approach, SpringerS Srivastava, RK Garg, VS Sharma, A SachdevaArchives of Computational Methods in Engineering, 2021•Springer 28 (2021) 3491–3515. doi: 10.1007/s11831-020-09511-4.
[53] A. Nycz, Y. Lee, M. Noakes, D. Ankit, C.M.-M.& Design, undefined 2021, Effective residual stress prediction validated with neutron diffraction method for metal large-scale additive manufacturing, ElsevierA Nycz, Y Lee, M Noakes, D Ankit, C Masuo, S Simunovic, J Bunn, L Love, V OanceaMaterials & Design, 2021•Elsevier (n.d.). https://www.sciencedirect.com/science/article/pii/S026412752100304X (accessed October 22, 2024).
[54] B. Ahmad, X. Zhang, H. Guo, M.E. Fitzpatrick, L.M.S.C. Neto, S. Williams, Influence of Deposition Strategies on Residual Stress in Wire + Arc Additive Manufactured Titanium Ti-6Al-4V, Metals (basel) 12 (2022), https://doi.org/10.3390/met12020253.